



Published in final edited form as:

IEEE Trans Med Imaging. 2015 October ; 34(10): 2058–2078. doi:10.1109/TMI.2015.2418674.

Estimating diffusion propagator and its moments using directional radial basis functions

Lipeng Ning, Carl-Fredrik Westin, and Yogesh Rathi

Brigham and Women's Hospital, Harvard Medical School, Boston, MA 02115

Lipeng Ning: lning@bwh.harvard.edu; Carl-Fredrik Westin: westin@bwh.harvard.edu; Yogesh Rathi: yogesh@bwh.harvard.edu

Abstract

The ensemble average diffusion propagator (EAP) obtained from diffusion MRI (dMRI) data captures important structural properties of the underlying tissue. As such, it is imperative to derive an accurate estimate of the EAP from the acquired diffusion data. In this work, we propose a novel method for estimating the EAP by representing the diffusion signal as a linear combination of directional radial basis functions scattered in q -space. In particular, we focus on a special case of anisotropic Gaussian basis functions and derive analytical expressions for the diffusion orientation distribution function (ODF), the return-to-origin probability (RTOP), and mean-squared-displacement (MSD). A significant advantage of the proposed method is that the second and the fourth order moment tensors of the EAP can be computed explicitly. This allows for computing several novel scalar indices (from the moment tensors) such as mean-fourth-order-displacement (MFD) and generalized kurtosis (GK) – which is a generalization of the mean kurtosis measure used in diffusion kurtosis imaging. Additionally, we also propose novel scalar indices computed from the signal in q -space, called the q -space mean-squared-displacement (QMSD) and the q -space mean-fourth-order-displacement (QMFD), which are sensitive to short diffusion time scales. We validate our method extensively on data obtained from a physical phantom with known crossing angle as well as on in-vivo human brain data. Our experiments demonstrate the robustness of our method for different combinations of b -values and number of gradient directions.

I. Introduction

Diffusion-weighted Magnetic Resonance Imaging (dMRI) is increasingly used to study the neural architecture and connectivity of the brain. It has proven important in clinical settings for investigating many brain disorders such as Alzheimer's disease, schizophrenia, mild traumatic brain injury etc. [1], [2], [3]. The ensemble average diffusion propagator (EAP), which describes the average displacement of spins within a voxel during the sampling period, provides important structural information of the underlying tissue. Thus, it is important to derive a reliable method to estimate the propagator from noisy measurements.

In the narrow pulse setting (for single pulse field gradient experiment), the EAP, denoted by $P(\mathbf{r})$, is related to the normalized diffusion signal $E(\mathbf{q}) \triangleq S(\mathbf{q})/S(0)$ measured in the q -space via the Fourier transform:

$$P(\mathbf{r}) = \int_{\mathbf{q} \in \mathbb{R}^3} E(\mathbf{q}) \exp(-i2\pi \mathbf{q} \cdot \mathbf{r}) d\mathbf{q}, \quad (1)$$

as given in [4], where \mathbf{r} is the displacement vector, and $S(\mathbf{q})$ is the diffusion signal measured at q-space point \mathbf{q} . The vector \mathbf{q} in the q-space is an experimentally controlled parameter with $\mathbf{q} = (2\pi)^{-1} \gamma \delta \mathbf{G}$ where, γ is the gyromagnetic ratio and δ is the duration of the diffusion sensitizing gradients whose magnitude and orientation are determined by the vector \mathbf{G} . Alternatively, E can be written as a function of b-value and a unit vector $\mathbf{u} \in \mathbb{S}^2$, such that $E(b, \mathbf{u}) : \mathbb{R}^+ \times \mathbb{S}^2 \rightarrow [0, 1]$, where $b = \gamma^2 \delta^2 (- \delta/3) \|\mathbf{G}\|^2$ s/mm² with τ being the mixing time (i.e., the time between two diffusion-encoding gradients). The fundamental relation given in Eq. (1) implies that $P(\mathbf{r})$ is uniquely determined by $E(\mathbf{q})$ which is measured directly in experiments. Thus, the propagator estimation problem reduces to one of estimating a continuous function $E(\mathbf{q})$ based on scattered measurements acquired in the q-space.

A classical method in dMRI is Diffusion Tensor Imaging (DTI) [5], which assumes that $E(\mathbf{q})$ is a Gaussian function centered at the origin ($\mathbf{q} = 0$). However, this over-simplified assumption has limitations in voxels where there is complex fiber architecture (crossing and kissing fiber bundles). To resolve this issue, High Angular Resolution Diffusion Imaging (HARDI) technique is nowadays becoming standard, which involves acquiring diffusion signal on a single q-shell in several gradient directions [6]. This protocol, in conjunction with various estimation methods [7], [8], [9], [10], is capable of resolving complex angular structures. However, it does not provide information about the signal decay along radial directions (with increasing q-value) which is desirable in studying subtle anomalies of white matter [11], [12].

The q-space imaging theory was first introduced by Paul Callaghan, see [13]. In practice, a imaging technique named Diffusion Spectrum Imaging (DSI) was recently introduced in [14], which involves acquiring measurements over a dense Cartesian grid of points in the q-space, followed by application of discrete Fourier transform to obtain an estimate of the EAP. However, a large number of measurements and a long acquisition time makes it impractical to use DSI in clinical settings. To address this issue, many imaging methods have been proposed, which reduce the number of measurements by using suitable signal models or by representing the signal using a series of functions in q-space [15], [16], [17], [18], [19]. For example, the Bessel Fourier basis [20], the Spherical Polar Fourier (SPF) basis [21], [22] and the spherical ridgelet basis [23] extend the spherical representation of the signal on a single shell to multiple shells with a continuous radial term. On the other hand, MAP-MRI [24] represents the diffusion signal using a combination of Hermite polynomials. Another related work is that of [25], where a linear combination of isotropic Sinc functions scattered in q-space, were used to represent the diffusion signal in q-space. This method is similar in spirit to our work, however the radial basis functions used are substantially different between the two methods. Further, we present several closed form analytical expressions for higher order moments of the EAP using the proposed method, whereas such expressions have not been derived for the Sinc basis functions.

In this work, we use directional radial basis functions for representing the diffusion signal and computing the corresponding EAP. In particular, the diffusion signal is expressed as a

linear combination of anisotropic Gaussian basis functions centered at several locations in the q -space. This is in contrast to other mixture models, which typically center the basis functions at the origin in q -space, e.g. [9]. Since the Fourier transform of a Gaussian is another Gaussian, one obtains simple analytical expressions for the EAP, and other quantities derived from the EAP, such as, the orientation distribution function (ODF) and the return-to-the-origin probability (RTOP). Moreover, a significant advantage of the proposed method is that the second order and fourth order moment tensors of the EAP can be computed explicitly, from which we can compute scalar indices such as mean-squared-displacement (MSD), mean-fourth-order-displacement (MFD), generalized kurtosis (GK) and many others. These measures capture higher order statistics of the diffusion propagator (and the q -space signal), which are particularly sensitive to the hindered and restricted components of the diffusion process. We extensively validate our method on a physical phantom data set with known fiber crossing and on an in-vivo human brain data set. Experiments on in-vivo human brain data demonstrate the different properties captured by our novel scalar indices, which could potentially be helpful in investigating subtle abnormalities in the brain tissue. Additionally, we also demonstrate the robustness of our technique to faithfully recover these diffusion measures from a sparse set of measurement, thus allowing for reducing the scan time.

II. Theory

A. Radial basis functions

A radial basis function (RBF) $\phi(\mathbf{x})$ with $\mathbf{x} \in \mathbb{R}^d$ is a real-valued function whose value at \mathbf{x} depends only on its distance to the origin. In the case of Euclidean distance, $\phi(\mathbf{x})$ can be written as $\phi(\|\mathbf{x}\|)$. RBF's are typically used for functional approximations of the form

$$s(\mathbf{x}) = \sum_{n=1}^N w_n \phi(\|\mathbf{x} - \mathbf{c}_n\|), \quad (2)$$

where the function to be approximated, $s(\mathbf{x})$, is represented as a sum of N radial basis functions each associated with a different center \mathbf{c}_n and a weighting coefficient w_n . A fundamental theorem derived in [26] shows that, if the function ϕ is continuous and bounded such that $\int_{\mathbb{R}^d} \phi(\mathbf{x}) = 0$, then the function $s(\mathbf{x})$ written in the form of (2) is dense in $L^p(\mathbb{R}^d)$ (which is the set of p^{th} power integrable functions). In other words, for a sufficiently large number N and suitably chosen centers \mathbf{c}_n 's, the radial basis functions can be used to approximate any well-behaved function up to any degree of precision. Hence, RBF's are widely used in many modern applications to approximate multivariate functions [27], [28].

A type of commonly used radial basis function is a Gaussian: $\phi(\mathbf{x}) = \exp(-\sigma\|\mathbf{x}\|^2)$ where, the normalization term is omitted since it can be absorbed into the weights, and $\|\mathbf{x}\|$ denotes the Euclidean distance from \mathbf{x} to the origin. In many situations, the so-called Mahalanobis distance is used instead of the Euclidean distance [29]. In general, a Mahalanobis distance between two points $\mathbf{x}, \mathbf{y} \in \mathbb{R}^d$ is defined by a positive definite matrix Σ , and is given by:

$$\|\mathbf{x} - \mathbf{y}\|_{\Sigma} = \sqrt{(\mathbf{x} - \mathbf{y})^T \Sigma (\mathbf{x} - \mathbf{y})}. \text{ Hence, the corresponding radial basis function } \phi(\mathbf{x}) = \exp(-\|\mathbf{x}\|_{\Sigma}^2) \text{ is a (scaled) multivariate Gaussian.}$$

B. Application in dMRI

We adapt the methodology of RBF's to represent the dMRI signal continuously in the q -space. Let $\{\mathbf{q}_1, \dots, \mathbf{q}_N\}$ be N fixed points (chosen *a-priori*) that are densely scattered in q -space which are also the centers of RBF's. We represent the normalized diffusion signal using

$$E(\mathbf{q}) = \sum_{n=0}^N w_n \phi_n(\mathbf{q} - \hat{\mathbf{q}}_n), \quad (3)$$

with $\phi_n(\mathbf{q} - \hat{\mathbf{q}}_n) = \exp(-(\mathbf{q} - \hat{\mathbf{q}}_n)^T D_n (\mathbf{q} - \hat{\mathbf{q}}_n))$ and $\mathbf{q}_0 = \hat{\mathbf{0}}$. This representation can also be thought of as a generalization of a scheme that involves placing all the basis functions at the **origin**. However, using a non-centered set of Gaussians allows for better modeling the signal decay at high q -value. Further, the theory of radial basis functions provides theoretical guarantees on the ability of such a framework to be able to represent any function with high accuracy [28].

The tensor D_0 is computed as in standard DTI [5] and the tensors D_n 's with $n \geq 1$ are assumed to have a cylindrical shape, which have the same set of eigenvectors as D_0 and with eigenvalues $\sigma_0, \sigma_1, \sigma_2$ such that $\sigma_1 = \sigma_2$. This anisotropic shape of D_n is motivated from the fact that the signal $E(\mathbf{q})$ decays faster along the direction indicated by the principle eigenvector of D_0 . While the eigenvectors of D_n could, theoretically, be set to random orientations, however, utilizing the orientation of D_0 could aid in better estimation of the signal decay. We should note that, even though the orientation of D_n is fixed to that of D_0 , yet, by an appropriate choice of the weights w_n , one can represent any type of anisotropic function to a very high degree of accuracy [27]. Moreover, using the eigenvectors of D_0 for D_n also leads to simpler expressions for several scalar statistics as shown in Appendix C-A. We note that without the first term $w_0 \phi_0(\mathbf{q})$, Eq. (3) is a standard radial basis function approximation problem. This extra term at the origin provides better fit for measurements from gray matter and CSF areas where signal decays almost isotropically along all directions.

Since the dMRI measurements are assumed to have antipodal symmetry i.e., $E(\mathbf{q}) = E(-\mathbf{q})$, we impose equal weights for Gaussian functions placed at antipodal pairs of points:

$$E(\mathbf{q}) = \sum_{n=0}^N w_n [\phi_n(\mathbf{q} - \hat{\mathbf{q}}_n) + \phi_n(\mathbf{q} + \hat{\mathbf{q}}_n)]. \quad (4)$$

The weights w_n 's are typically computed such that the mean squared error between $E(\mathbf{q})$ and the measurements is minimized. Given these weights, the estimated signal can be interpolated continuously in the q -space. An advantage of using Gaussian basis functions for representing the measured signal is that its Fourier transform, namely the EAP, can be computed analytically.

C. Estimation of EAP and ODF

Since the reconstructed signal $E(\mathbf{q})$ is a linear combination of Gaussian functions, its Fourier transform is given by a linear combination of the Fourier transforms of the individual basis functions. Hence, the estimated EAP, $P(\mathbf{r})$, is of the form

$$P(\mathbf{r}) = \mathcal{F}(E(\mathbf{q})) = \sum_{n=0}^N w_n \Phi_n(\mathbf{r}), \quad (5)$$

with $\Phi_n = \mathcal{F}(\varphi_n(\mathbf{q} - \mathbf{q}_n) + \varphi_n(\mathbf{q} + \mathbf{q}_n))$, where \mathcal{F} denotes the Fourier transform. In particular, the Fourier transform of the Gaussian function $\varphi_n(\mathbf{q})$ is given by

$$\int_{\mathbb{R}^3} \exp(-i2\pi\mathbf{q} \cdot \mathbf{r}) \exp(-\mathbf{q}^T D_n \mathbf{q}) d\mathbf{q} = \pi^{\frac{3}{2}} |D_n|^{-\frac{1}{2}} \exp(-\pi^2 \mathbf{r}^T D_n^{-1} \mathbf{r}).$$

A translation of a basis function leads to a phase shift of its Fourier transform, i.e. $\mathcal{F}(\varphi_n(\mathbf{q} + \mathbf{q}_n \hat{\mathbf{n}})) = \exp(i2\pi\mathbf{q}_n \hat{\mathbf{n}} \cdot \mathbf{r}) \mathcal{F}(\varphi_n(\mathbf{q}))$. Hence,

$$\Phi_n(\mathbf{r}) = 2\pi^{\frac{3}{2}} |D_n|^{-\frac{1}{2}} \cos(2\pi\hat{\mathbf{q}}_n \cdot \mathbf{r}) \exp(-\pi^2 \mathbf{r}^T D_n^{-1} \mathbf{r}). \quad (6)$$

Though each individual $\Phi_n(\mathbf{r})$ has exponentially decayed oscillation, a combination of many basis functions may provide a positive diffusion propagator (at least within a large range of \mathbf{r}) with suitable constraints for the diffusion signal, see Section VI for more detail.

In dMRI, the orientational feature of the underlying tissue can be visualized by using the diffusion orientation distribution function (ODF), which is the marginal of the propagator $P(\mathbf{r})$ on the unit sphere. More specifically, the (solid angle version) ODF, denoted by $\Psi(\mathbf{u})$, is computed from the EAP by evaluating the integral

$$\Psi(\mathbf{u}) = \int_0^\infty P(r\mathbf{u}) r^2 dr,$$

where \mathbf{u} is a unit vector and r is the radial co-ordinate [14]. From the propagator $P(\mathbf{r})$, $\Psi(\mathbf{u})$ can be computed analytically as $\Psi(\mathbf{u}) = \sum_{n=0}^N w_n \Psi_n(\mathbf{u})$, with $\Psi_n(\mathbf{u}) = \int_0^\infty \Phi_n(r\mathbf{u}) r^2 dr$ which is given by

$$\Psi_n(\mathbf{u}) = \frac{1}{2\pi} |D_n|^{-\frac{1}{2}} (\mathbf{u}^T D_n^{-1} \mathbf{u})^{-\frac{3}{2}} \left(1 - \frac{2(\mathbf{u} \cdot \hat{\mathbf{q}}_n)^2}{\mathbf{u}^T D_n^{-1} \mathbf{u}} \right) \times \exp \left(-\frac{(\mathbf{u} \cdot \hat{\mathbf{q}}_n)^2}{\mathbf{u}^T D_n^{-1} \mathbf{u}} \right). \quad (7)$$

We provide more details for Ψ_n in Appendix A.

One significant advantage of the proposed method is that the moments of the EAP can be computed explicitly. These moments provide statistics that describe important features of the underlying tissue. Thus, they can be potentially used in investigating tissue

abnormalities. Let $\mathbf{r} = [x \ y \ z]^T$ denote the displacement vector and $\gamma \triangleq \mathbf{r} \otimes \mathbf{r} \in \mathbb{R}^9$, where \otimes denotes the Kronecker product. Then the covariance matrix of \mathbf{r} is defined as

$$R \triangleq \int_{\mathbb{R}^3} \mathbf{r} \mathbf{r}^T P(\mathbf{r}) d\mathbf{r}, \quad (8)$$

which is a 3×3 positive definite matrix whose eigenvectors determine the principal diffusion directions. The diagonal entries of R are the mean-squared displacements along the x , y and z directions, respectively. Moreover, the fourth order diffusion tensor is given by

$$M \triangleq \int_{\mathbb{R}^3} \gamma \gamma^T P(\mathbf{r}) d\mathbf{r}.$$

Explicit expressions for R and M are given in Appendix B.

III. Scalar indices derived from the EAP

In this section, we discuss some quantitative scalar indices that could be used to describe various features of the underlying diffusion process. We also provide closed form expressions for these indices.

A. Mean-squared-displacement (MSD) and mean-fourth-order-displacement (MFD)

The mean-squared-displacement (MSD) is proportional to the average amount of diffusion that occurs during the diffusion experiment. It can be computed from the following expression:

$$\text{MSD} = \int_{\mathbb{R}^3} \|\mathbf{r}\|^2 P(\mathbf{r}) d\mathbf{r} = \text{trace}(R).$$

The last equality follows from (8) and the fact that $\|\mathbf{r}\|^2 = \text{trace}(\mathbf{r} \mathbf{r}^T)$, where $\text{trace}(\cdot)$ denotes the trace operator. Similarly, the mean-fourth-order-displacement (MFD), which is defined as

$$\text{MFD} = \int_{\mathbb{R}^3} \|\mathbf{r}\|^4 P(\mathbf{r}) d\mathbf{r} = \text{trace}(M),$$

can be computed from the fourth order moment tensor M . This measure is more sensitive to the “tail” of the diffusion propagator, and hence it can capture contributions from the hindered components of the diffusion propagator.

B. Hindered and restricted diffusivity

In standard DTI, the diffusion of water molecules is modeled by a Gaussian propagator $G(\mathbf{r})$ with a covariance matrix $R_g = \frac{1}{2\pi^2} D_0$. However, the diffusion in human brain tissue is typically restricted or hindered, making the diffusion propagator non-Gaussian [30], [31]. The amount of hindered and restricted diffusivity can be captured by computing the discrepancy between the estimated propagator $P(\mathbf{r})$ and the Gaussian propagator $G(\mathbf{r})$. For this purpose, we compute an angular metric between $P(\mathbf{r})$ and $G(\mathbf{r})$ as in [24].

1) Non-Gaussianity (NG)—Consider two propagators $P(\mathbf{r})$ and $Q(\mathbf{r})$ with their inner product defined as $\langle P(\mathbf{r}), Q(\mathbf{r}) \rangle = \int_{\mathbb{R}^3} P(\mathbf{r})Q(\mathbf{r})d\mathbf{r}$. Suppose $P(\mathbf{r})$ and $Q(\mathbf{r})$ are expressed in the form of (5) with the weighting coefficients given by w_n and v_n for $n = 0, \dots, N$, respectively.

Then the inner product can be written as $\langle P(\mathbf{r}), Q(\mathbf{r}) \rangle = \sum_{m=0}^N \sum_{n=0}^N w_n v_n T_{mn}$ where

$$T_{mn} = \langle \Phi_m(\mathbf{r}), \Phi_n(\mathbf{r}) \rangle = 2(\langle \phi_m(\mathbf{q} - \hat{\mathbf{q}}_m), \phi_n(\mathbf{q} - \hat{\mathbf{q}}_n) \rangle + \langle \phi_m(\mathbf{q} - \hat{\mathbf{q}}_m), \phi_n(\mathbf{q} + \hat{\mathbf{q}}_n) \rangle)$$

with the second equality obtained from Parseval's theorem and the inner product between two basis functions $\phi_m(\mathbf{q} - \hat{\mathbf{q}}_m)$

$$\begin{aligned} \langle \phi_m(\mathbf{q} - \hat{\mathbf{q}}_m), \phi_n(\mathbf{q} - \hat{\mathbf{q}}_n) \rangle &= \pi^{\frac{3}{2}} |D_m + D_n|^{-\frac{1}{2}} \exp \left(\right. \\ &\quad - \hat{\mathbf{q}}_m^T D_m \hat{\mathbf{q}}_m \\ &\quad - \hat{\mathbf{q}}_n^T D_n \hat{\mathbf{q}}_n \\ &\quad \left. + (D_m \hat{\mathbf{q}}_m + D_n \hat{\mathbf{q}}_n)^T (D_m + D_n)^{-1} (D_m \hat{\mathbf{q}}_m \right. \\ &\quad \left. + D_n \hat{\mathbf{q}}_n) \right). \end{aligned} \quad (9)$$

Similar to the method used in [24], the angular metric between the two propagators is defined as

$$\cos \theta_{PQ} = \frac{\langle P(\mathbf{r}), Q(\mathbf{r}) \rangle}{(\langle P(\mathbf{r}), P(\mathbf{r}) \rangle \langle Q(\mathbf{r}), Q(\mathbf{r}) \rangle)^{\frac{1}{2}}}.$$

In terms of the representation coefficients in the basis functions, the angular metric is given by the expression

$$\cos \theta_{PQ} = \frac{\sum_{m=0}^N \sum_{n=0}^N w_n v_n T_{mn}}{\left(\sum_{m=0}^N \sum_{n=0}^N w_m w_n T_{mn} \sum_{m=0}^N \sum_{n=0}^N v_m v_n T_{mn} \right)^{\frac{1}{2}}} \quad (10)$$

Consequently, a dissimilarity measure can be defined as $\sin \theta_{PQ} = \sqrt{1 - \cos^2 \theta_{PQ}}$ which takes value between 0 and 1. In practice, one may want to scale the value of the dissimilarity measures in order to obtain better contrast. For this purpose, we used the same family of functions as in [24] which is given by $\sigma(t, \varepsilon) = t^{3\varepsilon} / (1 - 3t^\varepsilon + 3t^{2\varepsilon})$ where t is the value to be scaled, e.g. $t = \sin \theta_{PQ}$, and the parameter $\varepsilon > 0$. The non-Gaussianity (NG) of the diffusion of water molecules is reflected by the dissimilarity between the estimated EAP $P(\mathbf{r})$ and the Gaussian propagator $G(\mathbf{r})$. To this end, the value of $\cos \theta_{PG}$ is given by

$$\cos \theta_{PG} = \frac{\sum_{m=0}^N w_m T_{m0}}{\left(\sum_{m=0}^N \sum_{n=0}^N w_m w_n T_{mn} T_{00} \right)^{\frac{1}{2}}}.$$

We define the non-Gaussianity (NG) as

$$\text{NG} \triangleq \sigma(\sin\theta_{PG}, \varepsilon)$$

and throughout this paper we use $\varepsilon = 0.4$ as in [24].

2) Difference in covariances—As a distance measure between the diffusion propagators, NG reflects the difference in all the moments of the estimated EAP and a Gaussian propagator. Since the higher order moments of the EAP are determined by the higher order derivatives of the diffusion signal near the origin, they are usually more sensitive to measurement noise. Consequently, a distance measure between only the second order moments R and R_g may be used to measure the hindered or the restricted diffusion though it only partially reflects the difference between the propagators. In the following, we present two methods for comparing the second order moments.

Let $\hat{\mathbf{r}}$ denote the displacement of molecules that is distributed according to a zero-mean Gaussian function $G(\mathbf{r})$. If the propagator is non-Gaussian, each displacement vector $\hat{\mathbf{r}}$ is associated with a difference in displacement $\tilde{\mathbf{r}}$ such that the true displacement $\hat{\mathbf{r}} + \tilde{\mathbf{r}}$ actually has a covariance matrix R (as opposed to R_g). There are many ways to account for the difference in displacement, which could lead to the covariance matrix R . One choice is based on the theory of optimal mass transport, and is also closely related to the Wasserstein metric for comparing probability measures [32]. This measure, which we define as a measure of Difference in Covariances is given by:

$$\text{DC} \triangleq \min_{\tilde{\mathbf{r}}} \int_{\mathbb{R}^3} \|\tilde{\mathbf{r}}\|^2 G(\mathbf{r}) d\mathbf{r},$$

such that the covariance matrix of $\hat{\mathbf{r}} + \tilde{\mathbf{r}}$ is R . DC has a closed form expression in terms of R and R_g , (see e.g. [33], [34]) and is given by:

$$\text{DC} = \text{trace} \left(R + R_g - 2 \left(R_g^{\frac{1}{2}} R R_g^{\frac{1}{2}} \right)^{\frac{1}{2}} \right).$$

DC measures the difference in the second moment of the diffusion propagator which partially reflects the hindrance or restriction on the diffusing molecules.

Alternatively, a symmetric comparison of the relative difference between R and R_g can be computed using $\text{trace} (R^{-1} R_g + R_g^{-1} R) - 6$. Based on the inequality $x + \frac{1}{x} \geq 2$ with $x > 0$, it can be easily shown that this distance measure is nonnegative and it equals to zeros if and only if $R = R_g$. In practice, we expect that both this distance measure and DC have similar contrast between tissues, however the relative distance may be more sensitive to noise due to the matrix inversion. To this end, we only consider DC in the experiments of the paper.

3) Generalized Kurtosis (GK)—A multivariate generalization of kurtosis was studied in [35] and is given by

$$\text{GK} \triangleq \langle (\mathbf{r}^T R^{-1} \mathbf{r})^2 \rangle_P = \int_{\mathbb{R}^3} (\mathbf{r}^T R^{-1} \mathbf{r})^2 P(\mathbf{r}) d\mathbf{r},$$

where R is the moment tensor (covariance matrix) of the diffusion propagator $P(\mathbf{r})$. It can be easily shown that, if $P(\mathbf{r})$ is a Gaussian distribution function, then $\text{GK} = 15$. Thus, $\text{GK} > 15$ implies that $P(\mathbf{r})$ has a fatter tail than a Gaussian and is called super-Gaussian. On the other hand, sub-Gaussian diffusion leads to $\text{GK} < 15$. In our framework, GK can be easily computed from: $\text{GK} = \mathbf{y}^T M \mathbf{y}$ where $\mathbf{y} \in \mathbb{R}^9$ is obtained by packing all the columns of R^{-1} into a vector. Thus, this measure has a specific range of scalar values that can be used to interpret the type of the diffusion propagator (Gaussian, sub-Gaussian, super-Gaussian), unlike the “mean kurtosis” measure typically used in the literature [36].

Since MSD and MFD are the second and the fourth order moments of the ℓ_2 -norm $\|\mathbf{r}\|$ of the displacement, respectively, an alternative way of generalizing the mean kurtosis is to compare MFD and $(\text{MSD})^2$. To this end, we define the Generalized Kurtosis of the Norm (GKN) of displacement as

$$\text{GKN} \triangleq \frac{\langle \|\mathbf{r}\|^4 \rangle_P}{\langle \|\mathbf{r}\|^2 \rangle_P^2} = \frac{\text{MFD}}{(\text{MSD})^2}.$$

If $P(\mathbf{r})$ is Gaussian, GKN measures the anisotropy of the diffusion process. In particular, it can be shown that $\text{GKN} = 5/3$, if $P(\mathbf{r})$ is isotropic Gaussian, and it equals to 3 for a completely anisotropic Gaussian. If $P(\mathbf{r})$ is not a Gaussian, then the fatter tail of $P(\mathbf{r})$ leads to higher values for GKN.

Since both GK and GKN reflect the kurtosis of the computed propagator, we expect them to have similar contrast between different tissue types. We also note that though the definition of GK is practically less attractive, as it is usually more sensitive to the measurement noise because it needs the computation of a matrix inversion. A quick comparison between these moment based measures and the one obtained by computing the difference between the entire propagators (NG), is that, the measures such as GK and GKN have specific numerical ranges that make it intuitive to understand the physical meaning behind the estimated numbers.

Similar to the scalar statistics derived for the EAP, explicit expressions for the moments of q-space signal also provides several important indices that characterize different properties of the underlying tissue. In Appendix C, we provide explicit expressions for the return-to-origin probability (RTOP), the return-to-the-axis probability (RTAP), the return-to-the-plane probability (RTPP), the q-space mean-squared displacement (QMSD) and the q-space mean-fourth-order-displacement (QMFD).

IV. Estimation method

The first step in the estimation procedure is to fix the parameters of the radial basis functions. In this work, the radial basis functions are parameterized by the tensors D_n 's and the centers $\hat{\mathbf{q}}_n$'s. As was explained earlier, the tensors D_n 's (at each voxel) have the same eigenvectors as that of D_0 , which in turn is estimated using a standard tensor fitting technique as in DTI. Note that, the eigenvalues for D_n are different from that of D_0 and are fixed a-priori. On the other hand, the centers $\hat{\mathbf{q}}_n$'s, for $n=1, \dots, N$, are chosen as a set of dense points in q-space (for all voxels). In the examples of this paper, we chose $N = 162$ and the centers are distributed on two b-shells along 81 gradients. A detailed description for choosing these parameters is presented in Section V-B. We note that once the basis functions have been defined, the EAP, the ODF and the moments are all a function of the weights w_n . Thus the performance of the proposed method heavily relies on the strategy used in estimating these coefficients. In this section, we discuss different methods for computing the coefficients w_n 's.

Given K measurements of $E(\mathbf{q})$ at $\{\mathbf{q}_1, \dots, \mathbf{q}_K\}$, we denote $\mathbf{e} \in \mathbb{R}^{K \times 1}$ as the vector of measurements, i.e. $e_k = E(\mathbf{q}_k)$ for $k = 1, \dots, K$. From the Gaussian basis functions, one constructs a $K \times (N + 1)$ dimensional matrix A with

$$A_{k,n+1} = \phi_n(\mathbf{q}_k - \hat{\mathbf{q}}_n) + \phi_n(\mathbf{q}_k + \hat{\mathbf{q}}_n)$$

for $n = 0, \dots, N$. We denote by \mathbf{w} , a vector of size $N + 1$ whose entries are the coefficients w_n (to be estimated). Typically, the vector \mathbf{w} can be estimated such that the mean squared error between $A\mathbf{w}$ and \mathbf{e} is minimized.

Since the linear system $A\mathbf{w} = \mathbf{e}$ may be underdetermined in cases when only a small number of measurements are available, a simple method is to estimate \mathbf{w} as a solution of the Tikhonov regularization problem

$$\min_{\mathbf{w}} \|A\mathbf{w} - \mathbf{e}\|^2 + \lambda \|\mathbf{w}\|^2$$

with $\lambda > 0$ being the weighting coefficient. This optimization problem has a closed form solution given by $\mathbf{w}_{\ell_2} = (A^T A + \lambda I)^{-1} A^T \mathbf{e}$.

More recently, the ℓ_1 regularization method has been shown to be useful in solving linear inverse problems especially when the vector \mathbf{w} is assumed to be sparse. In this case, \mathbf{w} is estimated as the solution of the optimization problem:

$$\min_{\mathbf{w}} \|A\mathbf{w} - \mathbf{e}\|^2 + \lambda \|\mathbf{w}\|_1.$$

This minimization approach, however, does not take into account the decay of the diffusion signal with increasing q-value. Several authors have reported that the observed signal with increasing b-values shows a multi-exponential type of decay (or a power-law decay) [30], [31], [37]. Hence, we assume that *the diffusion measurements are monotonically decreasing*

with increasing b -values. Moreover, the diffusion signal should be positive and the value of the measurement (normalized) at the origin is known to be one. Thus, one can numerically enforce these constraints while estimating the weight vector \mathbf{w} by solving the following optimization problem:

$$\begin{aligned} \min_{\mathbf{w}} \quad & \|A\mathbf{w} - \mathbf{e}\|^2 + \lambda \|\mathbf{w}\|^2 \\ \text{s. t.} \quad & B\mathbf{w} \geq 0, \mathbf{c}^T \mathbf{w} = 1. \end{aligned} \quad (11)$$

The matrix B is of the form $B = [B_1^T, B_2^T]^T$ with each column of B_1 being ϕ_n evaluated at a given set of locations for \mathbf{q} and each column of B_2 being the difference between the ϕ_n 's along a given set of gradient directions at several b -value shells. Specifically, we choose a set of points on X shells with b -values $b = b_1, \dots, b_X$ and $b_1 \ b_2 \ \dots \ b_X$. On each b -value shell, we use Y points along the directions $\mathbf{u}_1, \dots, \mathbf{u}_Y$. Hence, the total number of points is XY . We denote these points as $\mathbf{q}_{x,y}$ for $x = 1, \dots, X$ and $y = 1, \dots, Y$. The matrix B_1 has size $XY \times (N + 1)$ and each column of B_1 is the value of the basis function at the chosen set of XY points. In particular, the (xy, n) th element of B_1 is given by

$$B_1(xy, n) = \phi_{n-1}(\mathbf{q}_{x,y} - \hat{\mathbf{q}}_{n-1}) + \phi_{n-1}(\mathbf{q}_{x,y} + \hat{\mathbf{q}}_{n-1}),$$

for $x = 1, \dots, X, y = 1, \dots, Y$ and $n = 1, \dots, N + 1$. The matrix B_2 has size $(X - 1)Y \times (N + 1)$ and the $xy \times n$ the entry of B_2 is given by

$$B_2(xy, n) = B_1(xy, n) - B_1((x+1)y, n),$$

for $x = 1, \dots, X-1, y = 1, \dots, Y$ and $n = 1, \dots, N + 1$. Each entry in the vector \mathbf{c} is the value of basis function at the origin, i.e. $\mathbf{c}_{n+1} = 2\phi_n(\hat{\mathbf{q}}_n)$. We note that these constraints are always feasible and a trivially feasible element is given by $\mathbf{w} = [1, 0, \dots, 0]^T$.

V. Experiments

We tested our method on a data set acquired from a spherical physical phantom as shown in Figure 1a with a crossing angle of 45 degree. The phantom was developed along the same lines as described in [38]. Grooves of size $1 \times 0.7 \text{ cm}^2$ were filed with polyfil fibers of diameter $15 \text{ }\mu\text{m}$. The fibers were dipped in NaCl solution during the winding process to potentially remove air between fibers. After the winding, the phantom was immediately placed into a bin and its position was fixed by casting it into agarose gel.

The data sets were acquired on a 3T Siemens scanner with voxel size of $2 \times 2 \times 7 \text{ mm}^3$. We acquired 10 separate scans of the phantom with 5 different b -values with $b = \{1000, 2000, 3000, 4000, 5000\} \text{ s/mm}^2$ and each b -value shell consisted of 81 gradient directions. The 10 scans were averaged to obtain the ‘‘gold-standard’’ data. The experimental parameters for $b = 5000 \text{ s/mm}^2$ were as follows: $\|\mathbf{G}\| = 20.79 \text{ mT/m}$, $TE/TR = 141/3400 \text{ ms}$ and $\delta \approx 62 \text{ ms}$. The FOV was 118×54 and in-plane GRAPPA acceleration factor of 2 was used during

image acquisition. The color coded FA and the B_0 images of the data set are shown in Figure 1b and 1c, respectively.

The test data set was based on one slice of the physical phantom and was acquired as follows: For each of the following number of gradient directions $K = \{16, 20, 24, 30, 36, 42, 60, 81\}$, we acquired the diffusion measurement over 2 b-shells corresponding to $b = \{1000, 3000\} \text{ s/mm}^2$ and $b = \{1000, 2000\} \text{ s/mm}^2$, respectively. Further, 5 repetitions were acquired for each of these data samples to test the effect of noise on signal reconstruction quality. For data sets with the same number of gradient directions, we compute the signal-to-noise ratio

(SNR) for signal $S_r(\mathbf{q})$ at the r th voxel at \mathbf{q} as $\frac{\text{Mean}(\{S_r^k(\mathbf{q}), k=1, \dots, 5\})}{\text{STD}(\{S_r^k(\mathbf{q}), k=1, \dots, 5\})}$ where STD denotes the standard deviation. The average SNR over all gradient directions and over all data sets is considered the SNR in the corresponding voxel. Table I shows the average SNR in different voxels with different b-values.

A. Comparison metrics

We demonstrate the performance of our method on different number of measurements as well as on different b-values using the following comparison metrics.

a) Normalized mean-squared error (NMSE) in signal reconstruction—Let \hat{e}_x denote the reconstructed signal at location \mathbf{x} that is estimated at the same points in q-space as the “gold-standard” signal $e_{x,\text{gold}}$. The normalized mean squared error (NMSE) in signal reconstruction was computed using

$$\text{NMSE} = \frac{1}{|\Omega|} \sum_{\mathbf{x} \in \Omega} \frac{\|\hat{e}_x - e_{x,\text{gold}}\|^2}{\|e_{x,\text{gold}}\|^2},$$

where Ω denotes the set of all voxel locations and $|\Omega|$ is the total number of voxels. Thus, lower NMSE implies that the reconstructed signal is close to the “gold-standard” signal.

b) Estimated angle (EA)—The orientation of the fibers at each voxel location is indicated by the peaks of the estimated ODF. These peaks are often used in tractography methods to determine the connectivity of the brain. Thus, accurate estimation of the ODF peaks is important in studying white matter fiber bundles. For the case of the phantom data set, the fiber crossing was at a known angle of 45° . The estimated angle (EA) was computed at each of the voxels where a crossing of two fibers was detected.

The estimated angle between the two principal diffusion directions (in case of crossing) was computed as the average estimated angle (EA) given by

$$\text{EA} = \frac{1}{|\Omega_2|} \sum_{\mathbf{x} \in \Omega_2} |\arccos(\mathbf{u}_{x,1} \cdot \mathbf{u}_{x,2})|,$$

where $\mathbf{u}_{x,1}$ and $\mathbf{u}_{x,2}$ denote the direction of the two peaks at location \mathbf{x} and Ω_2 denotes the set of locations that have two peaks.

c) Percentage of false peaks (PFP)—The estimated angle was computed only at those locations where two peaks were detected. However, in many cases, the recovered signal may miss or overestimate the number of peaks. Thus, the percentage of false peaks (PFP) is used to evaluate the accuracy of peak detection with respect to the gold standard. Based on the results from gold-standard data set, two sets of voxels were selected such that $\Omega_{\text{gold},1}$ contained only those voxels with one peak, while $\Omega_{\text{gold},2}$ contained all voxels with two crossing fibers. For each set, the percentage of false peaks (PFP) was computed using:

$$\text{PFP}(i) = \frac{1}{|\Omega_{\text{gold},i}|} \sum_{\mathbf{x} \in \Omega_{\text{gold},i}} \mathcal{B}(n_{\mathbf{x}} - i), \text{ for } i=1, 2,$$

where $n_{\mathbf{x}}$ denotes the number of peaks detected at location \mathbf{x} and \mathcal{B} is a binary function whose value is 1 if $n_{\mathbf{x}} = i$ and 0 otherwise.

d) NMSE in estimation of scalar statistics—Let $P_{\mathbf{x}}(0)$ denote the estimated return-to-origin probability (RTOP) and $P_{\text{gold},\mathbf{x}}(0)$ be the estimated RTOP for the gold-standard data, both computed using the same method (ℓ_1 regularized, 3D-SHORE etc.). The normalized mean-squared error in the estimation of RTOP is computed using

$$\text{NMSE of RTOP} = \frac{1}{|\Omega|} \sum_{\mathbf{x} \in \Omega} \frac{\|P_{\mathbf{x}}(0) - P_{\text{gold},\mathbf{x}}(0)\|^2}{\|P_{\text{gold},\mathbf{x}}(0)\|^2}.$$

The normalized-mean-squared-errors for RTAP, RTPP, MSD, MFD, MMSDE, NG, DC, GK, GKN, QMSD and QMFD were defined in a similar fashion.

B. Implementation details

We used these metrics to quantify the reconstruction quality of the data using the anisotropic Gaussian basis functions. All the three methods discussed in the previous section, i.e. the ℓ_1 regularized, ℓ_2 regularized and ℓ_2 regularized with constraints, were used to estimate the representation vector \mathbf{w} . The centers $\hat{\mathbf{q}}_n$ of Gaussian basis function were uniformly distributed on two b-value shells with $b = \{2000, 4000\}$ along 81 gradient directions on the hemisphere. Thus, $N = 162$ and the total number of columns of the basis matrix A was 163. We note that the location of center points could vary for different acquisition schemes. Following the theory of radial basis functions [28], as long as the center points are densely placed in q-space and enough measurements are available, the fitted signal will be an accurate estimate of the true signal. In our experiments, we used the same set of $\hat{\mathbf{q}}_n$'s in all the examples (for dense and sparsely sampled data, both in-vivo and phantom) to show the robustness of our choice of the center points. For the ℓ_2 regularized methods, the parameter λ was chosen such that the condition number of $A^T A + \lambda I$ is bounded by 10^7 . This bound is chosen to be large enough so that λ is small and the estimated signal is mainly determined by the least-squares fitting term in the objective function. For the method using ℓ_2 regularization with constraints, the signal was constrained to be non-negative along 81 gradient directions uniformly sampled on the hemisphere. Along each gradient direction, the

difference in the signal at the b-value shells $\{1000, 2000, \dots, 8000\} \text{ s/mm}^2$ were constrained to be non-negative. The eigenvalues for the Gaussian basis functions φ_n were set to $\sigma_0 = 0.0011 \text{ mm}^2/\text{s}$, $\sigma_1 = 0.0006 \text{ mm}^2/\text{s}$ for the ℓ_2 and ℓ_1 regularization methods, while for the constrained ℓ_2 regularization method, the parameters were set to $\sigma_0 = 0.0015 \text{ mm}^2/\text{s}$ and $\sigma_1 = 0.0008 \text{ mm}^2/\text{s}$. These parameters were selected using an exhaustive search, so that the estimated angle with 30 gradient directions was as close as possible to the ground truth. *We should however emphasize that, we used the same set of parameters for all sampling schemes and data sets, to demonstrate the robustness of the proposed method. Further, the training data set was different than the test data set used to obtain the optimal parameters (σ_0, σ_1).*

We compared the proposed methods with the 3D-SHORE method of [19]. In this case, we constructed the basis matrix A according to the 3D-SHORE basis functions and estimated the coefficient vector using ℓ_1 regularization [19], ℓ_2 regularization [39], [19], ℓ_2 regularization with the constraints for monotonicity and positivity of the signal (for a fair comparison with our Gaussian basis function based method). The scale parameter of 3D-SHORE basis and the regularization coefficients were chosen as described in [19].

C. Phantom results

Our main goal in studying phantom data is to quantitatively evaluate the performance of the different estimation methods. Moreover, by comparing the estimation results we can also determine the most economical sampling scheme for the proposed method. In particular, if the measurements are to be sampled on two b-value shells with $b = \{1000, 3000\}$, what is the trade off between the performance and the acquisition time? If the scan time allows to acquire only 60 measurements, should we use b-values with $b = \{1000, 2000\}$ or use $b = \{1000, 3000\}$ and 30 directions each? The extensive validation we perform in this work is an attempt to answer these questions using the proposed methods.

The estimation results on the “gold standard” data (where the actual angle is 45°) with different methods are summarized in Table II:

The estimated ODF’s with gold-standard data using the six methods are shown in Figure 7 in Appendix D. All the six methods successfully detected the crossing fibers based on the gold-standard data set. In Figure 7d and Figure 7f, the top-left and bottom-right corners of the glyph’s are not displayed since the estimated ODF’s have negative values in these isotropic regions.

We first compared our results using the test data set with $b = \{1000, 3000\}$ and the number of gradient directions $K = \{16, 20, 24, 30, 36, 42, 60, 81\}$. For visual inspections, Figure 8 in Appendix D shows the estimated ODF’s using one data set with 30 gradient directions on each shell (60 total measurements). In particular, the figures on the left panel are obtained using the proposed Gaussian basis methods and the results obtained using 3D-SHORE are shown on the right. For the gold-standard data set, as was shown in Figure 7, all the methods successfully identified the crossing fibers. However, with fewer number of samples, the performance of the 3D-SHORE basis methods deteriorated. Many voxels in the crossing region in Figure 8b, 8d and 8f did not detect the fiber crossing.

1) Estimated angle—The orientation of the fibers is estimated via the peaks of the ODF. A maxima of the ODF is considered as a valid peak if its value is at-least 40% of the highest peak in that ODF. Considering the fact that the estimated ODF's may have small spurious peaks (see Figure 7f and Figure 8e), this threshold of 40%, was chosen so that these artifacts do not lead to a significant number of incorrect detection in the 3D-SHORE method.

Numerically, the ODF is evaluated on a grid of 2562 points sampled on the sphere. If there are only two peaks detected, the directions corresponding to the peaks are used to compute the estimated angle in that voxel. The average estimated angles for the six methods are shown in Figure 2a. We note that if the number of gradient directions is larger than 30, the estimated angle using all the three Gaussian basis function based methods (red curves) are within 1.5° of the ground truth. Results also show that, the ℓ_2 regularization method with 3D-SHORE basis underestimated the angle with fewer number of samples. The angle obtained using ℓ_1 3D-SHORE method is within 2° of the ground truth for $K = 30$.

2) Percentage of false peaks—We note that *the estimated angles were computed only at voxels in the region of crossing fibers where two peaks were detected in the ODF*. To get a complete picture, it is important to compute the percentage of voxels with the correct number of peaks. We computed the percentage of false peaks (PFP) in the region with and without crossing fibers separately.

Figure 2b shows the percentage of false peaks in the region with two fiber crossings. We observe that among the proposed methods, ℓ_2 Gaussian with constraints, has the lowest error rate which is around 4% with 30 gradient directions and is about 11% with 24 gradient directions. The two unconstrained methods using ℓ_1 regularization and ℓ_2 regularization for Gaussian basis functions have similar performances but slightly higher error than the constrained method. On the other hand, all the three methods using 3D-SHORE basis functions have much higher percentage of false peaks. Among those methods, the ℓ_1 regularization based method leads to better results than the other two. Note that, the proposed method performs significantly advantage in detecting the correct number of peaks than the 3D-SHORE method.

Figure 2c shows the percentage of false peaks in the region of one-fiber voxels. In this case, the ℓ_1 and ℓ_2 regularized Gaussian methods have slightly higher error (about 8%). The constrained ℓ_2 Gaussian method however has better performance (about 6% false positives), similar to the 3D-SHORE basis methods.

3) Normalized-mean-squared-errors (NMSE)—Figure 9a in Appendix D shows the NMSE of the reconstructed signal *with respect to the gold-standard data*. The method using ℓ_2 Gaussian with constraints has the lowest fitting error which is about 1.5% with 30 gradient directions. The ℓ_2 3D-SHORE with constraints has lower NMSE compared with the other two 3D-SHORE based methods. We note that the performances of both methods, Gaussian and 3D-SHORE have been improved by using the constraints. In order to compare the difference between the estimated signal obtained by Gaussian with constraints and 3D-SHORE with constraints, Figure 3 shows the radial profile (signal as a function of b-value) of the estimated and the gold-standard signal. The first and second row of Figure 3 show the

signal in a single-fiber and two-fiber voxel, respectively. Each line in these figures corresponds to the signal along one gradient directions at different b-values. Clearly, all the signals are positive and monotonically decreasing along radial directions, though the signal may seem to be flat along some directions. We also note that the estimated signal obtained by ℓ_2 Gaussian with constraints at high b-values, i.e. at $b = 4000, 5000 \text{ s/mm}^2$, is quite similar to gold standard, which is the main reason that the proposed method (Gaussian with constraints) has lower NMSE and better angular performance.

The NMSE of the return-to-the-origins-probability (RTOP) is computed by comparing the estimated RTOP obtained using gold-standard data for each of the methods and the results are shown in Figure 9b. We note that ℓ_2 Gaussian with constraints performs significantly better than other methods whose NMSE in RTOP is about 1.5%. The ℓ_1 Gaussian and ℓ_2 Gaussian methods have similar performance with about 7% error for 30 directions. The NMSE in RTOP for the two ℓ_2 regularized 3D-SHORE basis based methods are all above 50% while for ℓ_1 regularization it is 80%. This further demonstrates that the 3D-SHORE method does not model the high b-value signal correctly and greatly emphasizes the low b-value data, resulting in poor estimate of RTOP. We should emphasize that, the “gold standard” data contains b-values up to 5000, whereas the test data had b-values of only 1000 and 3000. Thus, higher error in RTOP is due to the fact that the 3D-SHORE method does not extrapolate the data correctly in the high b-value regime.

Since the scalar indices RTAP, RTPP, MSD, MFD, NG, DC, GK, GKN, QMSD and QMFD do not have a closed form expression using the 3D-SHORE methods, we only computed the corresponding normalized-mean-squared-errors using the Gaussian basis function methods as shown in Figure 9c to 9l. The method using ℓ_2 regularization and constraints has the lowest NMSE for RTAP, RTPP, MSD, MFD, NG, DC, QMSD and QMFD among the three methods. These three methods have similar values for NMSE in GK and GKN. We note that the NMSE in RTPP for ℓ_1 Gaussian is larger than 100% while the NMSE of RTPP for ℓ_2 Gaussian with constraints is about 1%.

4) Performance using only lower b-value data—We also tested the performance of all the six methods on data sets with two lower b-value shells with $b = \{1000, 2000\}$ and with the same number of gradient directions $K = \{16, 20, 24, 30, 36, 42, 60, 81\}$. The estimated angle and percentage of false peaks are shown in Figure 4. In particular, Figure 4b shows that the proposed methods using Gaussian basis functions performs better than the methods using 3D-SHORE basis in detecting multiple peaks. Comparing Figure 4b, 4c to Figure 2b and 2c, respectively, we note that the percentage of false peaks using $b = \{1000, 2000\}$ is higher than using $b = \{1000, 3000\}$.

The normalized-mean-squared-error of the reconstructed signal and RTOP for the six methods are shown in Figure 10a and 10b in Appendix D, respectively. The proposed Gaussian basis function based method using ℓ_2 regularization and constraints still has the best performance. The NMSE of RTAP, RTPP, MSD, MFD, NG, DC, GK, GKN, QMSD and QMFD for the three methods using Gaussian basis functions are shown in Figure 10c to 10l, respectively. These plots show similar relations among the three method as was shown in Figure 9. We summarize the normalized-mean-squared-errors using ℓ_2 Gaussian with

constraints for 30 gradient directions on two b-value shells with $b = \{1000, 2000\}$ and $b = \{1000, 3000\}$ in the following table: We note that all the normalized-mean-squared errors obtained using measurements on b-values shell with $b = \{1000, 2000\}$ are higher than the corresponding results based on $b = \{1000, 3000\}$. Hence, if the scan time only allows to acquire 60 measurements, for the proposed method, we recommend using measurements on b-value shells with $b = \{1000, 3000\}$ and 30 directions each.

These comparisons using phantom data suggest that the ℓ_2 Gaussian with constraints provides better performance than the other five alternatives. The comparisons also show that if the sampling time allows for 60 samples on b-value shells, a better choice is to sample the signal on the b-value shells of $b = \{1000, 3000\}$.

D. In vivo results

We tested our method on in-vivo human brain data with the following scan parameters on a 3T Siemens scanner: spatial resolution of $2.5\text{mm} \times 2.5\text{mm} \times 2.5\text{mm}$, b-values of $\{900, 2000, 3600, 5600\}\text{s/mm}^2$ with each b-value shell having 60 gradient directions. This data set was considered as the “gold-standard” data. The test data set was obtained by subsampling the gold-standard data on b-value shells with $b = \{900, 3600\}\text{s/mm}^2$ along 30 or 60 gradient directions on each shell. The experimental parameters were as follows: 32-channel head coil, GRAPPA acceleration factor of 2, maximum gradient strength of $\|\mathbf{G}\| = 31.62\text{ mT/m}$, $TE/TR = 141/3400\text{ ms}$ and $\delta = 45\text{ ms}$ and $\tau = 54\text{ ms}$. We used all the six methods to estimate the ODF’s for the voxels shown in the rectangular region (white box) in Figure 5g. *We used the same parameters for the Gaussian basis functions that were used for the phantom data set.*

The estimated ODF’s with the gold-standard data set and using the ℓ_2 Gaussian constraints, ℓ_2 3D-SHORE constraints and ℓ_1 3D-SHORE are shown in the left panel of Figure 5, while the right panel shows the corresponding results using the data set obtained on two b-value shells with $b = \{900, 3600\}$ and 30 gradient directions (total of 60 measurements). In each of the ODF glyphs, the estimated return-to-the-origin probabilities of each methods are shown in the background. Visually, the estimated ODFs shown in Figure 5a and Figure 5b are very similar with each other. The ODF’s are almost isotropic in voxels where the RTOP is low (dark background). For the ODF’s highlighted in the rectangular area, where three fiber crossing is detected in gold-standard data, we see that one of the fiber component is missing using the subsampled data; see 5b.

ODF profiles using 3D-SHORE is shown in Figure 5c and Figure 5d. Two of the voxels in the rectangle area of Figure 5d failed to detect some of the peaks. The ODF’s shown in Figure 5f are smoother and sharper than the ODF’s obtained by other methods. However, in the rectangular area of Figure 5c, three voxels failed to detect the correct number of peaks compared to gold standard data. The RTOP shown in Figure 5f are not consistent with the results shown in other figures due to poor extrapolation.

The comparison metrics for the test set with measurements on two b-value shells and 30 gradient directions (per shell) are tabulated in Table IV. The NMSE of the reconstructed signal is slightly higher than the results shown in the phantom data set indicating that the

SNR for in vivo data set is possibly even lower than the phantom data (SNR = 9.5). Further, we did not have several acquisitions of the same individual, hence the gold standard data itself was quite noisy. The normalized-mean-squared-errors obtained by the ℓ_2 Gaussian with constraints are consistently lower than the results using other methods. We note that due to low SNR and singularity in the denominator, the NMSE of DC for ℓ_2 and ℓ_1 Gaussian methods are higher than 100%.

We also computed the comparison metrics for the test set using measurement on two b-values shells and 60 gradient directions (120 total measurements) as shown in Table V. We note that there is no significant improvement in the performance by doubling the number of samples.

We also computed the scalar indices for one coronal slice of the brain as shown in Figure 11 in Appendix E using the gold-standard data set with the proposed Gaussian basis function based method with ℓ_2 regularization and constraints. The return-to-the-origin-probability (RTOP) shown in Figure 11a highlights the white matter areas including the regions with crossing fibers. The return-to-the-axis probability (RTAP) is shown in Figure 11b which shows the contrast between single-fiber white matters and the regions with crossing fibers. The return-to-the-plane probability (RTPP) is shown in Figure 11c which shows lower values in single-fiber white matter region corresponding to high diffusion along the fiber direction. Figure 11d shows the fractional anisotropy (FA) that is obtained from DTI. Figure 11e and Figure 11f are respectively the mean-squared-displacement (MSD) and mean-fourth-order-displacement (MFD), both showing similar contrast between gray/white and CSF areas. The ratio MFD/MSD^2 corresponds to the images shown in Figure 11j which is the generalized kurtosis of norm (GKN) estimated at each voxel.

The scalar indices that capture hindered diffusivity are shown in the third row of Figure 11. In particular, in Figure 11g, white matter areas which are more densely packed (e.g. corpus callosum, cortico-spinal tract) have higher non-Gaussianity (NG) than areas that have less densely packed fibers. Figure 11h also highlights the white matter areas but the contrast between white matter and gray matter areas is stronger than Figure 11g. Note that, areas of white matter that are affected by partial voluming due to adjoining gray matter or CSF areas also have lower DC.

Figure 11i shows the generalized kurtosis (GK). The values for gray matter and CSF areas are very close to 15 which indicate that the underlying diffusion process is similar to free Gaussian diffusion in these regions. The single-fiber white matter areas show higher GK than the crossing fiber areas. The GKN shown in Figure 11j also shows similar patterns as the generalized kurtosis. One important feature that these measures present is that, both GK and GKN are higher in densely packed white matter areas with predominantly single fiber bundles than in the crossing fiber areas, indicating that these measures provide different contrast than the standard mean kurtosis measure presented in [40]. Note that, the GKN values in the gray matter and CSF areas are very close to $5/3$ which is the value corresponding to isotropic Gaussian.

Figure 11k and Figure 11l are respectively the q-space mean-squared-displacement (QMSD) and q-space mean-fourth-order-displacement (QMFD). These two figures have similar contrast as the HD, although the underlying processes could be different (hindered vs restricted diffusion). Unlike MSD and MFD, these two images highlight the white-matter area while MSD and MFD are brighter in the CSF areas.

We also computed the same set of scalar indices using only measurements on two b-value shells with $b = \{900, 3600\}$ and 30 gradient directions per shell as shown in Figure 12 in Appendix E, respectively. These figures are all very similar to the corresponding results that are obtained for the gold-standard data set, albeit with slight error in the estimation of higher order statistics (GK, GKN). However, the overall contrast between different white and gray matter regions is similar to that of the gold standard data.

VI. Discussion and conclusion

In this work, we presented a novel method to represent and analyze diffusion MRI data from low to high b-value data. A framework using directional radial basis functions was introduced to estimate the three-dimensional q-space signal and the diffusion propagator (EAP) in analytical forms. The properties of the proposed method can be summarized in the following aspects:

- If the goal of a neuroimaging study is to obtain subtle measures of diffusion to obtain accurate micro structural information about the tissue, 60 measurements are needed spread over at least two b-shells ($b = 1000$ and $b = 3000$). Note that, a high b-value of 3000 is required for accurate estimation of several diffusion measures. We also note that the proposed method can be applied to diffusion data sets that have different gradient directions on multiple b-shells.
- An important feature of the proposed method using Gaussian basis functions is that many high order statistics, such as the return-to-the-origin probability, mean-squared-displacement, the second and the fourth order moment tensors of the propagator, can be computed in a stable and analytical manner. We also proposed several novel scalar indices that were derived from these higher order moment tensors, such as Generalized Kurtosis (GK) and the Generalized Kurtosis of the Norm (GKN) of the displacement. In particular, the GK considers the diffusion signal from the entire q-space (as opposed to the measure of kurtosis used in diffusion kurtosis imaging, which is only valid up to a maximum b-value of around 2500). Additionally, we proposed two high order statistical quantities computed from the q-space data, which are more sensitive to restricted diffusion. Further, we provided analytical formulations for quantities such as return-to-axis and return-to-plan probabilities.
- The proposed method allows analytical computation of the ODF and hence can be used within any tractography algorithm as well, but requires a slightly sophisticated acquisition scheme with multiple b-values. Thus, the proposed method is quite general and can be used in connectivity analysis as well as to study diffusion properties.

We have showed using experiments on human in-vivo data that the proposed scalar indices reveal different features of the nervous tissue structure. We also have performed extensive validation of our method on a physical phantom data set and demonstrated the robust performance of using the proposed method (Gaussian basis with constraints) on sub-sampled data sets. Hence, the proposed method can be potentially used to analyze dMRI data in neuroscience studies. Next, we discuss the limitations and some possible issues for applying our method in clinical settings.

As was shown in equation (6), each individual basis function in the r -space is an exponentially decaying oscillatory function. Though a linear combination of a large set of basis functions may reduce the oscillations, the computed EAP may not be monotonically decreasing along radial directions. For example, Figure 6 shows the radial profile of the estimated propagator in a single-fiber voxel of the phantom data set using measurements on the b-shells on $b = 1000, 2000 \text{ s/mm}^2$ along 30 directions. We note that the propagator is not monotonically decreasing along some of the fast-decay directions. Since the propagator was not enforced to be positive, we have observed that the propagator may have negative values in some data sets. Though small negative values did not lead to any significant issues in our experiments, we note that it may be useful to enforce positive constraints for the EAP in a similar way as in [24] when applying the proposed method in clinical settings to study brain disorders. In this case, we expect a larger number of basis functions to be used which will certainly increase the computational burden significantly. With our current settings, the computational time for a whole-brain data set is about 6-7 hours using 8 processes.

Another concern for using the proposed method in clinical settings is the choice of the basis parameters. The set of the parameters used in this paper were learned from a physical phantom data set so that they provide close-to-optimum performances for many data sets. The same set of parameters were also used for in-vivo data set from a healthy adult human brain. We have seen that the estimation result is robust with changes in the parameters, i.e. small difference in the parameters will not lead to significant variations in the estimated results. However, these parameters may not be optimal for neonate or infant brains.

The code base for the proposed method can be downloaded via the link <https://github.com/LipengNing/RBF-Propagator>. Some of the phantom data sets are also available at the website http://projects.iq.harvard.edu/sparcdmri/Challenge_Data.

Acknowledgments

The authors would like to acknowledge the following grants which supported this work: R01MH099797 (PI: Rathi), R01MH074794 (PI: Westin), P41EB015902 (PI: Kikinis), Swedish Research Council (VR) grant 2012-3682 and Swedish Foundation for Strategic Research (SSF) grant AM13-0090. We would also like to thank Dr. Frederik Laun from the German Cancer Research Center for providing the physical phantom data.

References

1. Thomason ME, Thompson PM. Diffusion imaging, white matter, and psychopathology. *Clinical Psychology*. 2011; 7(1):63.
2. Shenton M, Hamoda H, Schneiderman J, Bouix S, Pasternak O, Rathi Y, Vu MA, Purohit M, Helmer K, Koerte I, et al. A review of magnetic resonance imaging and diffusion tensor imaging

- findings in mild traumatic brain injury. *Brain imaging and behavior*. 2012; 6(2):137–192. [PubMed: 22438191]
3. Shi Y, Short SJ, Knickmeyer RC, Wang J, Coe CL, Ni-ethammer M, Gilmore JH, Zhu H, Styner MA. Diffusion tensor imaging–based characterization of brain neurodevelopment in primates. *Cerebral Cortex*. 2013; 23(1):36–48. [PubMed: 22275483]
 4. Stejskal E, Tanner J. Spin diffusion measurements: Spin echoes in the presence of a time-dependent field gradient. *The journal of chemical physics*. 1965; 42(1):288–292.
 5. Basser P, Mattiello J, LeBihan D. Estimation of the effective self-diffusion tensor from the NMR spin echo. *Journal of Magnetic Resonance, Series B*. 1994; 103(3):247–254. [PubMed: 8019776]
 6. Tuch D, Reese T, Wiegell M, Makris N, Belliveau J, Wedeen V. High angular resolution diffusion imaging reveals intravoxel white matter fiber heterogeneity. *Magnetic Resonance in Medicine*. 2002; 48(4):577–582. [PubMed: 12353272]
 7. Tuch DS. Q-ball imaging. *Magnetic Resonance in Medicine*. 2004; 52(6):1358–1372. [PubMed: 15562495]
 8. Alexander DC. Multiple-fiber reconstruction algorithms for diffusion MRI. *Annals of the New York Academy of Sciences*. 2005; 1064(1):113–133. [PubMed: 16394152]
 9. Jian B, Vemuri BC. A unified computational framework for deconvolution to reconstruct multiple fibers from diffusion weighted MRI. *IEEE Transactions on Medical Imaging*. 2007; 26(11):1464–1471. [PubMed: 18041262]
 10. Michailovich O, Rathi Y. On approximation of orientation distributions by means of spherical ridgelets. *IEEE Transactions on Image Processing*. 2010; 19(2):461–477. [PubMed: 19887312]
 11. Cohen Y, Assaf Y. High b-value q-space analyzed diffusion-weighted MRS and MRI in neuronal tissues—a technical review. *NMR in Biomedicine*. 2002; 15(7–8):516–542. [PubMed: 12489099]
 12. Assaf Y, Freidlin RZ, Rohde GK, Basser PJ. New modeling and experimental framework to characterize hindered and restricted water diffusion in brain white matter. *Magnetic Resonance in Medicine*. 2004; 52(5):965–978. [PubMed: 15508168]
 13. Callaghan, PT. *Principles of nuclear magnetic resonance microscopy*. Vol. 3. Clarendon Press; Oxford: 1991.
 14. Wedeen VJ, Hagmann P, Tseng WYI, Reese TG, Weisskoff RM. Mapping complex tissue architecture with diffusion spectrum magnetic resonance imaging. *Magnetic Resonance in Medicine*. 2005; 54(6):1377–1386. [PubMed: 16247738]
 15. Asselmlal HE, Tschumperlé D, Brun L, Siddiqi K. Recent advances in diffusion MRI modeling: Angular and radial reconstruction. *Medical image analysis*. 2011; 15(4):369–396. [PubMed: 21397549]
 16. Wu Y, Alexander A. Hybrid diffusion imaging. *NeuroImage*. 2007; 36(3):617–629. [PubMed: 17481920]
 17. Descoteaux M, Deriche R, Le Bihan D, Mangin JF, Poupon C. Multiple q-shell diffusion propagator imaging. *Medical image analysis*. 2011; 15(4):603–621. [PubMed: 20685153]
 18. Özarlan, E.; Koay, C.; Shepherd, T.; Blackb, S.; Basser, P. Simple harmonic oscillator based reconstruction and estimation for three-dimensional q-space MRI. *ISMRM 17th Annual Meeting and Exhibition*; Honolulu. 2009; p. 1396
 19. Merlet SL, Deriche R. Continuous diffusion signal, EAP and ODF estimation via compressive sensing in diffusion MRI. *Medical image analysis*. 2013; 17(5):556–572. [PubMed: 23602920]
 20. Hosseinbor AP, Chung MK, Wu Y-C, Alexander AL. Bessel fourier orientation reconstruction (bfor): An analytical diffusion propagator reconstruction for hybrid diffusion imaging and computation of q-space indices. *NeuroImage*. 2013; 64:650–670. [PubMed: 22963853]
 21. Asselmlal HE, Tschumperlé D, Brun L. Efficient and robust computation of PDF features from diffusion MR signal. *Medical Image Analysis*. 2009; 13(5):715–729. [PubMed: 19665917]
 22. Cheng, J.; Ghosh, A.; Jiang, T.; Deriche, R. *Medical Image Computing and Computer-Assisted Intervention–MICCAI 2010*. Springer; 2010. Model-free and analytical EAP reconstruction via spherical polar Fourier diffusion MRI; p. 590-597.
 23. Rathi, Y.; Michailovich, O.; Setsompop, K.; Bouix, S.; Shenton, ME.; Westin, C-F. *Medical Image Computing and Computer-Assisted Intervention–MICCAI 2011*. Springer; 2011. Sparse multi-shell diffusion imaging; p. 58-65.

24. Özarslan E, Koay CG, Shepherd TM, Komlosh ME, Orfanio M, Pierpaoli C, Basser PJ. Mean apparent propagator (MAP) MRI: A novel diffusion imaging method for mapping tissue microstructure. *NeuroImage*. 2013; 78:16–32. [PubMed: 23587694]
25. Ye W, Portnoy S, Entezari A, Blackband SJ, Vemuri BC. An efficient interlaced multi-shell sampling scheme for reconstruction of diffusion propagators. *IEEE Transactions on Medical Imaging*. 2012; 31(5):1043–1050. [PubMed: 22271832]
26. Park J, Sandberg IW. Universal approximation using radial-basis-function networks. *Neural computation*. 1991; 3(2):246–257.
27. Bishop, CM. *Neural networks for pattern recognition*. Oxford university press; 1995.
28. Buhmann, MD. *Radial basis functions: theory and implementations*. Vol. 12. Cambridge university press; 2003.
29. Schwenker F, Kestler HA, Palm G. Three learning phases for radial-basis-function networks. *Neural networks*. 2001; 14(4):439–458. [PubMed: 11411631]
30. Maier S, Vajapeyam S, Mamata H, Westin CF, Jolesz F, Mulkern R. Biexponential diffusion tensor analysis of human brain diffusion data. *Magnetic Resonance in Medicine*. 2004; 51(2):321–330. [PubMed: 14755658]
31. Niendorf T, Dijkhuizen RM, Norris DG, van Lookeren Campagne M, Nicolay K. Biexponential diffusion attenuation in various states of brain tissue: Implications for diffusion-weighted imaging. *Magnetic Resonance in Medicine*. 1996; 36(6):847–857. [PubMed: 8946350]
32. Villani, C. *Topics in optimal transportation*. Vol. 58. American Mathematical Society; 2003.
33. Knott M, Smith CS. On the optimal mapping of distributions. *Journal of Optimization Theory and Applications*. 1984; 43(1):39–49.
34. Ning L, Jiang X, Georgiou T. On the geometry of covariance matrices. *IEEE Signal Processing Letters*. 2013; 20(8):787.
35. Mardia KV. Measures of multivariate skewness and kurtosis with applications. *Biometrika*. 1970; 57(3):519–530.
36. Jensen JH, Helpert JA, Ramani A, Lu H, Kaczynski K. Diffusional kurtosis imaging: The quantification of non-gaussian water diffusion by means of magnetic resonance imaging. *Magnetic Resonance in Medicine*. 2005; 53(6):1432–1440. [PubMed: 15906300]
37. Bar-Shir A, Avram L, Özarslan E, Basser PJ, Cohen Y. The effect of the diffusion time and pulse gradient duration ratio on the diffraction pattern and the structural information estimated from q-space diffusion MR: Experiments and simulations. *Journal of Magnetic Resonance*. 2008; 194(2): 230–236. [PubMed: 18667345]
38. Moussavi-Biugui A, Stieltjes B, Fritzsche K, Semmler W, Laun FB. Novel spherical phantoms for Q-ball imaging under in vivo conditions. *Magnetic Resonance in Medicine*. 2011; 65(1):190–194. [PubMed: 20740652]
39. Assemlal, H-E.; Tschumperlé, D.; Brun, L. *Medical Image Computing and Computer-Assisted Intervention–MICCAI 2008*. Springer; 2008. Efficient computation of PDF-based characteristics from diffusion MR signal; p. 70-78.
40. Hansen B, Lund TE, Sangill R, Jespersen SN. Experimentally and computationally fast method for estimation of a mean kurtosis. *Magnetic Resonance in Medicine*. 2013; 69(6):1754–1760. [PubMed: 23589312]
41. Wu YC, Field AS, Alexander AL. Computation of diffusion function measures in q-space using magnetic resonance hybrid diffusion imaging. *IEEE Transactions on Medical Imaging*. 2008; 27(6):858–865. [PubMed: 18541492]
42. Hosseinbor, AP.; Chung, MK.; Wu, Y-C.; Fleming, JO.; Field, AS.; Alexander, AL. *Medical Image Computing and Computer-Assisted Intervention–MICCAI 2012*. Springer; 2012. Extracting quantitative measures from EAP: a small clinical study using BFOR; p. 280-287.

Appendix A. Derivations for the ODF

We provide the derivations of $\Psi_n(\mathbf{u})$ in (7) that is used for computing ODF. First, we compute the integral $\int_0^\infty 2\exp(-ax^2)\cos(bx)x^2 dx$ with $a > 0$, from which we can obtain the

expression for Ψ_n for specific values of a and b . Since the integrand $\exp(-ax^2) \cos(bx)x^2$ is symmetric with respect to the origin, the above integral equals to the real part of

$$\int_{-\infty}^{\infty} \exp(-ax^2 - ibx)x^2 dx. \quad (12)$$

By Cauchy's Integral Theorem, the integral of $\exp(-ax^2 - ibx)x^2$ along a rectangle with vertices at $-c$, c , $c - i\frac{b}{2a}$, $-c - i\frac{b}{2a}$ equals to zero. Letting $c \rightarrow \infty$, we see that (12) equals to

$$\int_{-\infty}^{\infty} \exp\left(-a\left(x - i\frac{b}{2a}\right)^2 - ib\left(x - i\frac{b}{2a}\right)\right) \left(x - i\frac{b}{2a}\right)^2 dx$$

whose real part can be easily computed as

$$\frac{1}{2} \pi^{\frac{1}{2}} a^{-\frac{3}{2}} \left(1 - \frac{b^2}{2a}\right) \exp\left(-\frac{b^2}{4a}\right). \quad (13)$$

Then the expression of $\Psi_n(\mathbf{u})$ in (7) can be obtained by multiplying $\pi^{\frac{3}{2}} |D_n|^{-\frac{1}{2}}$ to (13) and substituting a , b with $\pi^2 \mathbf{u}^T D_n^{-1} \mathbf{u}$ and $2\pi(\mathbf{u} \cdot \hat{\mathbf{q}}_n)$, respectively.

Appendix B. Second and fourth order moment tensors of EAP

A. Second order moment

Following (5), R has the expression $R = \sum_{n=0}^N w_n R_n$ where R_n is computed from the function Φ_n and is given by

$$R_n = \frac{1}{\pi^2} \exp(-\hat{\mathbf{q}}_n^T D_n \hat{\mathbf{q}}_n) \left(D_n - 2D_n \hat{\mathbf{q}}_n \hat{\mathbf{q}}_n^T D_n\right).$$

B. Fourth order moment

Using the proposed formulation, M can be estimated using $M = \sum_{n=0}^N w_n M_n$ with $M_n = \int_{\mathbb{R}^3} \gamma \gamma^T \Phi_n(\mathbf{r}) d\mathbf{r}$. Each element of the matrix M_n is of the form $\int_{\mathbb{R}^3} \mathbf{r}_i^2 \mathbf{r}_j \mathbf{r}_k \Phi_n(\mathbf{r}) d\mathbf{r}$ for $i, j, k \in \{1, 2, 3\}$ where \mathbf{r}_i denotes the i th element of \mathbf{r} . Due to symmetry in the indices, the 9×9 matrix M_n only has 15 independent elements. A general expression for each element can be derived explicitly and is given by:

$$\begin{aligned}
& \int_{\mathbb{R}^3} \mathbf{r}_i^T \mathbf{r}_j \mathbf{r}_k \Phi_n(\mathbf{r}) d\mathbf{r} = \\
& 2 \exp(-\hat{\mathbf{q}}_n^T D_n \hat{\mathbf{q}}_n) \left(\mu_i^2 \mu_j \mu_k - \frac{1}{2\pi^2} \mu_j \mu_k D_{n,ii} - \frac{1}{2\pi^2} \mu_i^2 D_{n,jk} \right. \\
& \quad \left. - \frac{1}{\pi^2} \mu_i \mu_k D_{n,ij} - \frac{1}{\pi^2} \mu_i \mu_j D_{n,ik} + \frac{1}{4\pi^4} D_{n,ii} D_{n,jk} \right. \\
& \quad \left. + \frac{1}{2\pi^4} D_{n,ij} D_{n,ik} \right)
\end{aligned}$$

where $\mu = \frac{1}{\pi} D_n \hat{\mathbf{q}}_n$ and $D_{n,ij}$ denotes the (i, j) th element of D_n . The matrices R and M provide higher order statistics of the diffusion propagator, from which, several useful scalar indices can be computed as described in the next section.

Appendix C. Statistics from Q-space

A. Return-to-the-origin probability (RTOP)

The net displacement of water molecules between the application of two diffusion sensitizing gradients is inversely proportional to the mean pore volume [24]. An estimate of this net displacement can be computed using the return-to-origin probability (RTOP), given by $P(0)$, which is the integral of the normalized diffusion signal over the entire q-space, i.e. $\text{RTOP} = \int_{\mathbb{R}^3} E(\mathbf{q}) d\mathbf{q}$. Following (5) and (6), the closed form expressions of the estimated RTOP is simply given by

$$P(0) = 2\pi^{\frac{3}{2}} \sum_{n=0}^N w_n |D_n|^{-\frac{1}{2}}.$$

In coherently organized white-matter, the diffusion is maximally restricted in the plane defined by the two smaller eigenvalues of the diffusion tensor (plane orthogonal to the main eigenvector). Therefore, [24] suggests to estimate the return-to-the-axis probability given by $\text{RTAP} = \int_{\mathbb{R}^2} E(\mathbf{q}_{\perp}) d\mathbf{q}_{\perp}$, where \mathbf{q}_{\perp} denotes a (RTAP) q-vector in the plane orthogonal to the principal diffusion direction. RTAP is the reciprocal of the mean cross-sectional area of the pore space. To derive the expression for RTAP using the proposed method, we let $\mathbf{u}_1, \mathbf{u}_2, \mathbf{u}_3$ be the eigenvectors of the tensor D_0 , associated with the three eigenvalues (in descending order). We note that in the proposed method, $\mathbf{u}_1, \mathbf{u}_2, \mathbf{u}_3$ are also the eigenvectors for D_n for n

1. Let σ_{n1}, σ_{n2} and σ_{n3} denote the three eigenvalues of D_n , such that $\sigma_{n1} \geq \sigma_{n2} \geq \sigma_{n3}$. Assuming \mathbf{u}_1 is the fiber orientation, the RTAP can be computed using

$$\text{RTAP} = 2\pi \sum_{n=0}^N w_n (\sigma_{n2} \sigma_{n3})^{-\frac{1}{2}} \exp(-\sigma_{n1} (\mathbf{u}_1 \cdot \hat{\mathbf{q}}_n)^2).$$

Similarly, the return-to-the-plane probability (RTPP) can be computed through a one-dimensional integral along the fiber orientation, i.e., $\text{RTPP} = \int_{\mathbb{R}} E(\mathbf{q}_{\parallel}) d\mathbf{q}_{\parallel}$, where \mathbf{q}_{\parallel} denotes the direction along the fiber axis. This measure is the inverse of the mean length of the cylinders. The expression for RTPP is given by

$$\text{RTPP} = 2\pi^{\frac{1}{2}} \sum_{n=0}^N w_n \sigma_{n1}^{-\frac{1}{2}} \exp(-\sigma_{n2}(\mathbf{u}_2 \cdot \hat{\mathbf{q}}_n)^2 - \sigma_{n3}(\mathbf{u}_3 \cdot \hat{\mathbf{q}}_n)^2).$$

It has been observed that the diffusion signal decay is biexponential in tissues with restricted compartments and small pore sizes [12]. Hence, the measurements in the high q -value regime are more sensitive to the restricted diffusion of water molecules. To this end, it is natural to derive the higher-order statistics of $E(\mathbf{q})$, i.e. $\int_{\mathbb{R}^3} \|\mathbf{q}\|^k E(\mathbf{q}) d\mathbf{q}$ for $k > 0$, in order to study the restricted diffusivity of the diffusion process. For $k = 0$, we obtain the return-to-the-origin probability $P(0)$. In the following, we introduce the second-order moment and the fourth-order moment tensors of the three-dimensional signal $E(\mathbf{q})$ using the proposed method.

B. Q-space mean-squared-displacement (QMSD)

Since the propagator is the Fourier transform of the diffusion signal, the higher order moments of the signal are equal to the higher order derivatives of the propagator at the origin scaled by certain constants. Thus, it would be informative to compute the higher order moments of the signal in q -space. The second-order moment tensor of $E(\mathbf{q})$ is defined as $R_q \triangleq \int_{\mathbb{R}^2} \mathbf{q}\mathbf{q}^T E(\mathbf{q}) d\mathbf{q}$ which is a 3×3 positive-semidefinite matrix. In the proposed method, R_q is estimated as

$$R_q = 2\pi^{\frac{3}{2}} \sum_{n=0}^N w_n |D_n|^{-\frac{1}{2}} \left(\frac{1}{2} D_n^{-1} + \hat{\mathbf{q}}_n \hat{\mathbf{q}}_n^T \right).$$

As an analogy to the mean-squared-displacement (MSD), we define the q -space mean-squared-displacement (QMSD) as

$$\text{QMSD} \triangleq \int_{\mathbb{R}^2} \|\mathbf{q}\|^2 E(\mathbf{q}) d\mathbf{q} = \text{trace}(R_q).$$

The reciprocal of QMSD was referred to as the q -space inverse variance (QIV) in [41], [42]. For Gaussian propagators, R_g equals to the inverse of the covariance R of $P(\mathbf{r})$. Hence, the inverse of QMSD has similar contrast as MSD in different tissue types. For non-Gaussian propagators, QMSD may have different contrast than MSD. Note that, other measures, such as anisotropy and norm of the matrix R_q can also be computed, to obtain more information about the covariance function of the signal in q -space.

C. Q-space mean-fourth-order-displacement (QMFD)

To introduce the fourth-order moment tensor, we define $\mathbf{p} = \mathbf{q} \otimes \mathbf{q} \in \mathbb{R}^9$. Then the fourth-order moment tensor of $E(\mathbf{q})$ is defined as $M_q \triangleq \int_{\mathbb{R}^3} \mathbf{p}\mathbf{p}^T E(\mathbf{q}) d\mathbf{q}$. In the proposed method,

M_q is estimated as $M_q = \sum_{n=0}^N w_n M_{q,n}$ with $M_{q,n} = \int_{\mathbb{R}^3} \mathbf{p}\mathbf{p}^T [\varphi_n(\mathbf{q} - \hat{\mathbf{q}}_n) + \varphi_n(\mathbf{q} + \hat{\mathbf{q}}_n)] d\mathbf{q}$ being

a symmetric matrix of size 9×9 . Each element of the matrix $M_{q,n}$ is of the form

$M_{q,n} = \int_{\mathbb{R}^3} \mathbf{p} \mathbf{p}^T [\phi_n(\mathbf{q} - \hat{\mathbf{q}}_n) + \phi_n(\mathbf{q} + \hat{\mathbf{q}}_n)] d\mathbf{q}$ for $i, j, k \in \{1, 2, 3\}$ where q_i denotes the i th element of \mathbf{q} . Due to symmetry in the indices, the 9×9 matrix $M_{q,n}$ only has 15 independent elements. The expression for $\int_{\mathbb{R}^3} q_i^2 q_j q_k [\phi_n(\mathbf{q} - \hat{\mathbf{q}}_n) + \phi_n(\mathbf{q} + \hat{\mathbf{q}}_n)] d\mathbf{q}$ is given as

$$\begin{aligned} & 2\pi^{\frac{3}{2}} |D_n|^{-\frac{1}{2}} (\hat{q}_{n,i}^2 \hat{q}_{n,j} \hat{q}_{n,k} + \frac{1}{2} \hat{q}_{n,j} \hat{q}_{n,k} (D_n^{-1})_{ii} \\ & + \frac{1}{2} \hat{q}_{n,i}^2 (D_n^{-1})_{jk} + \hat{q}_{n,i} \hat{q}_{n,k} (D_n^{-1})_{ij} + \hat{q}_{n,i} \hat{q}_{n,j} (D_n^{-1})_{ik} \\ & + \frac{1}{4} (D_n^{-1})_{ii} (D_n^{-1})_{jk} + \frac{1}{2} (D_n^{-1})_{ij} (D_n^{-1})_{ik}) \end{aligned}$$

where $q_{n,i}$ denotes the i th entry of $\hat{\mathbf{q}}_n$ and $(D_n^{-1})_{ij}$ denotes the (i, j) th element of D_n^{-1} . Similar to mean-fourth-order-displacement (MFD), we define the q-space mean-fourth-order-displacement (QMFD) as

$$\text{QMFD} \triangleq \int_{\mathbb{R}^2} \|\mathbf{q}\|^4 E(\mathbf{q}) d\mathbf{q} = \text{trace}(M_q).$$

We note that $E(\mathbf{q})$ is not a probability density function since its integral is not equal to one. Hence, the range for scalar indices introduced in Section III-B are not applicable to $E(\mathbf{q})$. Though we can still compute the scalar statistics in q-space using R_q and M_q , their values lie on the positive real line (without any bounds).

Both the measures introduced above, QMSD and QMFD, are more sensitive to slow diffusion compartments or restricted diffusion. This is in contrast to the measures derived from the diffusion propagator, which are more sensitive to hindered diffusion.

Appendix D. Experimental results using the phantom data sets

Figures 7 and 8 show the estimated ODF's for the phantom data sets. Figures 9 to 10 show the normalized-mean-squared errors.

Appendix E. Scalar statistics for the in vivo data sets

Figures 11 to 12 show the estimated scalar statistics for the in vivo data sets.

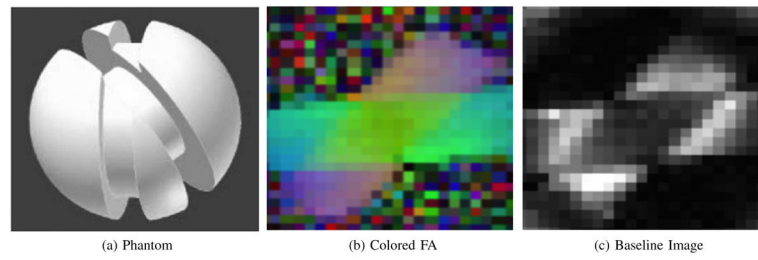


Fig. 1.

(a) The spherical phantom used for data acquisition. (b) The colored FA image of the data set used in SPARC. (c) The baseline image of the data set.

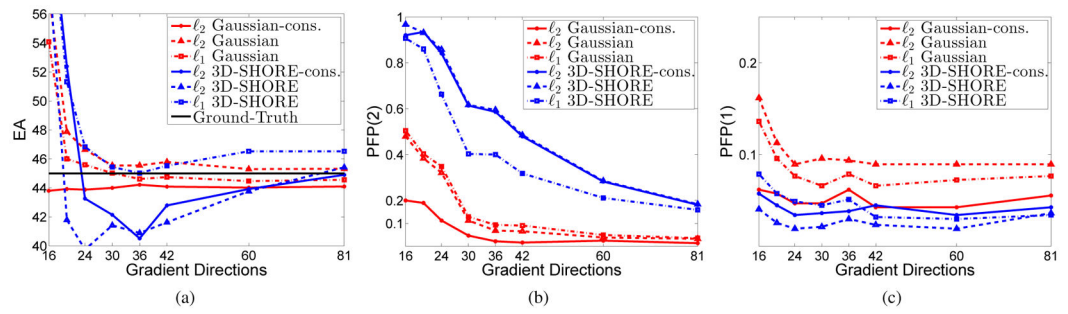


Fig. 2. Comparison metrics using measurements on b-value shells with $b = \{1000, 3000\}$ and gradient directions per shell (x-axis): (a) Estimated angle vs. gradient directions, (b) Percentage of false peaks for two-peak voxels vs. gradient directions, (c) Percentage of false peaks for one-peak voxels vs. gradient directions.

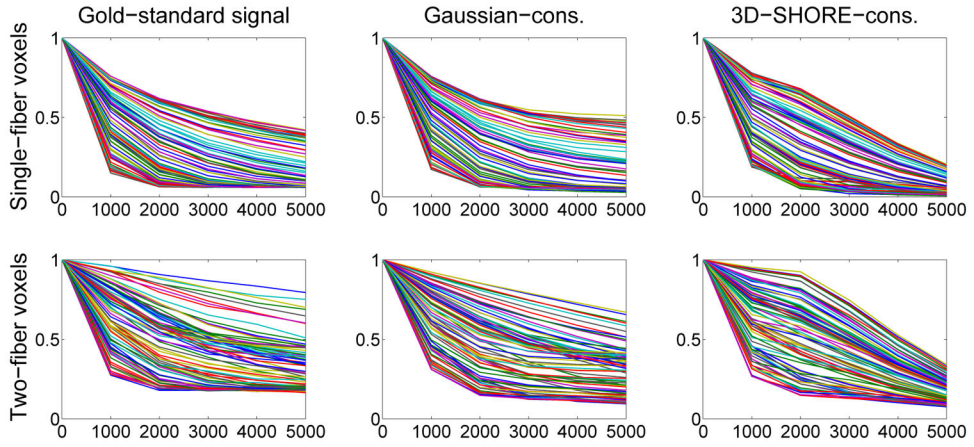


Fig. 3. The radial profile of the gold-standard signal, the estimated signals using ℓ_2 Gaussian with constraints and the estimated signal using ℓ_2 3D-SHORE with constraints, respectively. The estimated signal was based on measurements on b-shells with $b = 1000, 3000 \text{ s/mm}^2$ along 30 gradient directions. Each line in the figures corresponds to the diffusion signal along one gradient direction at different b-values.

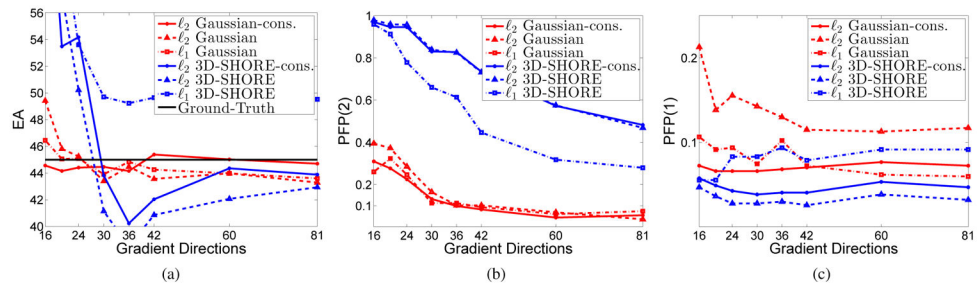


Fig. 4. Comparison metrics with measurements on b-value shells with $b = \{1000, 2000\}$: (a) Estimated angle vs. gradient directions, (b) Percentage of false peaks for two-peak voxels vs. gradient directions, (c) Percentage of false peaks for one-peak voxels vs. gradient directions.

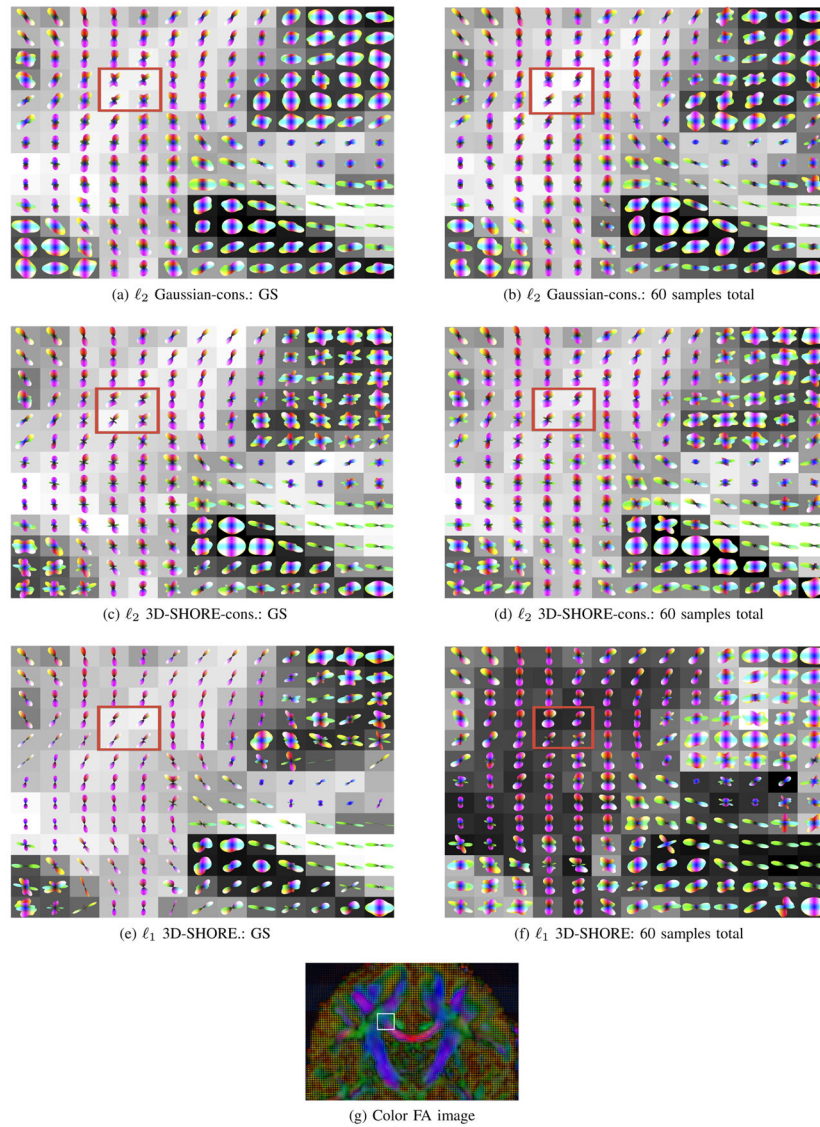


Fig. 5. Estimated ODF for the rectangle region in the color FA image (g). Left panel and right panel show respectively the results obtained from gold-standard (GS) data set and from measurements on two b-value shells with 30 gradient directions per shell (60 total).

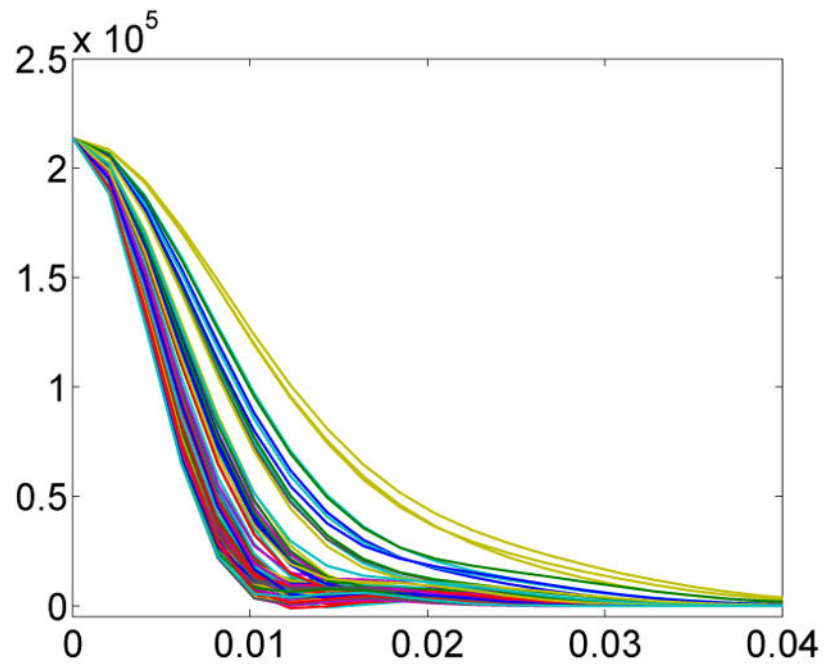


Fig. 6.
The radial profile of the estimated EAP is a single-fiber voxel of the phantom data set.

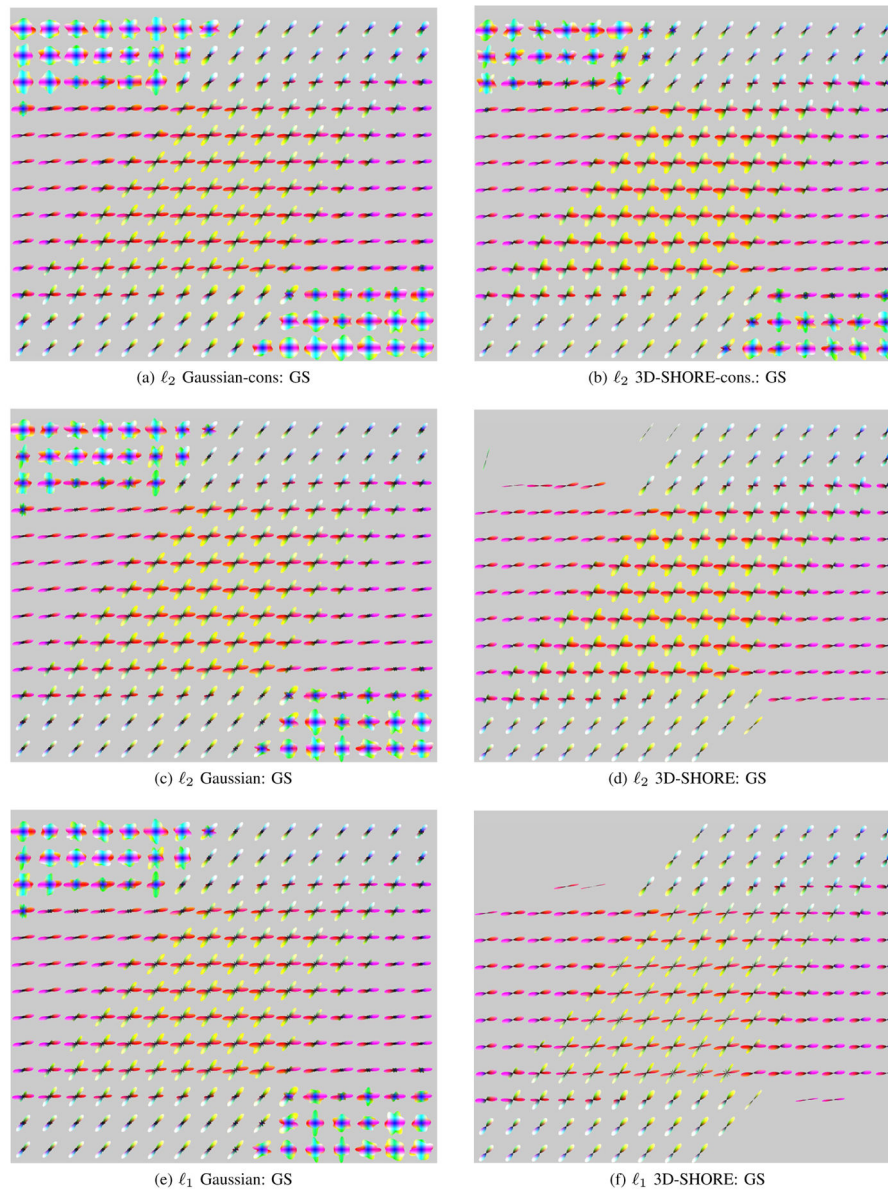


Fig. 7. Estimated ODF using “gold-standard” data: (a) Gaussian basis with ℓ_2 regularization and constraints, (b) 3D-SHORE basis with ℓ_2 regularization and constraints, (c) Gaussian basis with ℓ_2 regularization, (d) 3D-SHORE basis with ℓ_2 regularization, (e) Gaussian basis with ℓ_1 regularization, (f) 3D-SHORE basis with ℓ_1 regularization.

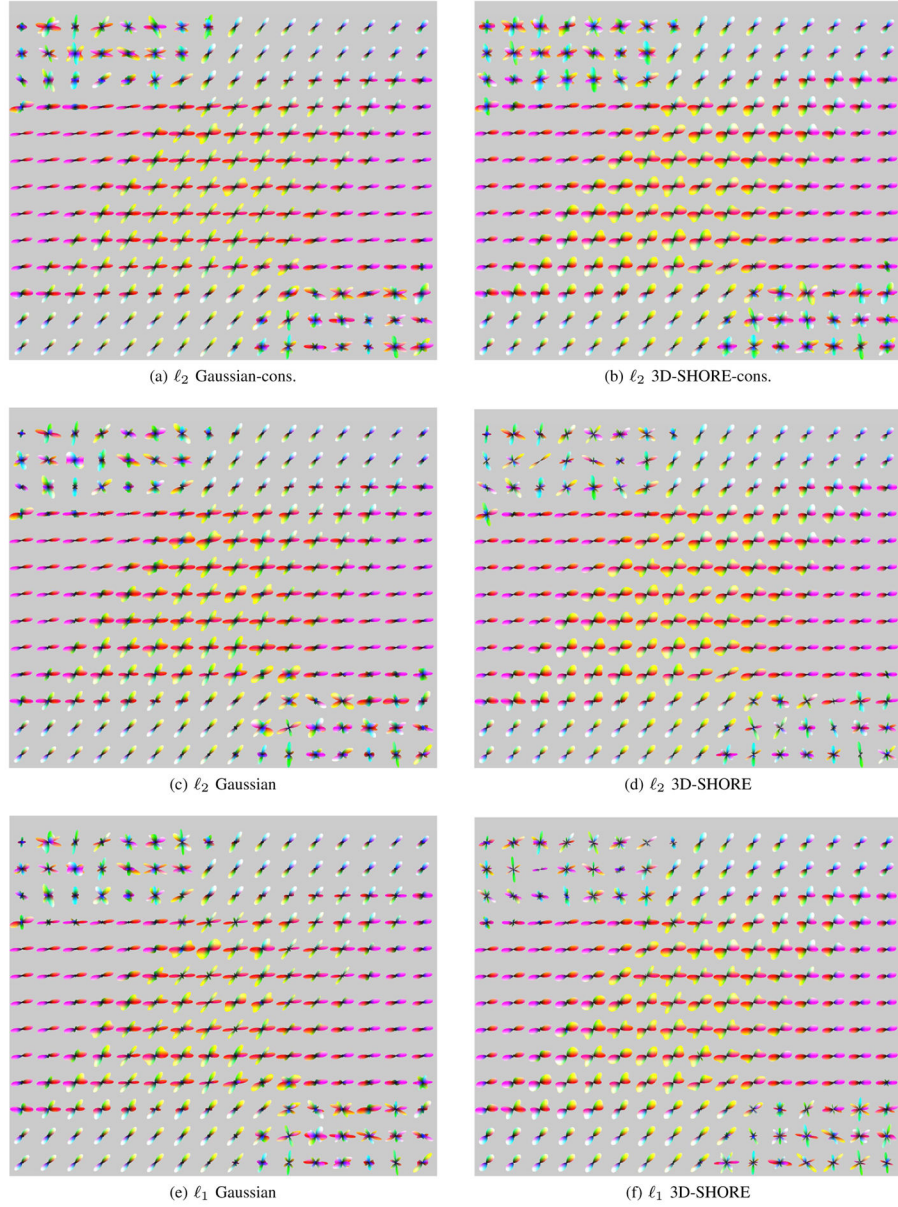


Fig. 8. Estimated ODF from measurements on b-value shells with $b = \{1000, 3000\}$ and with 30 gradient directions each (total of 60 measurements) using: (a) Gaussian basis with ℓ_2 regularization and constraints, (b) 3D-SHORE basis with ℓ_2 regularization and constraints, (c) Gaussian basis with ℓ_2 regularization, (d) 3D-SHORE basis with ℓ_2 regularization, (e) Gaussian basis with ℓ_1 regularization, (f) 3D-SHORE basis with ℓ_1 regularization

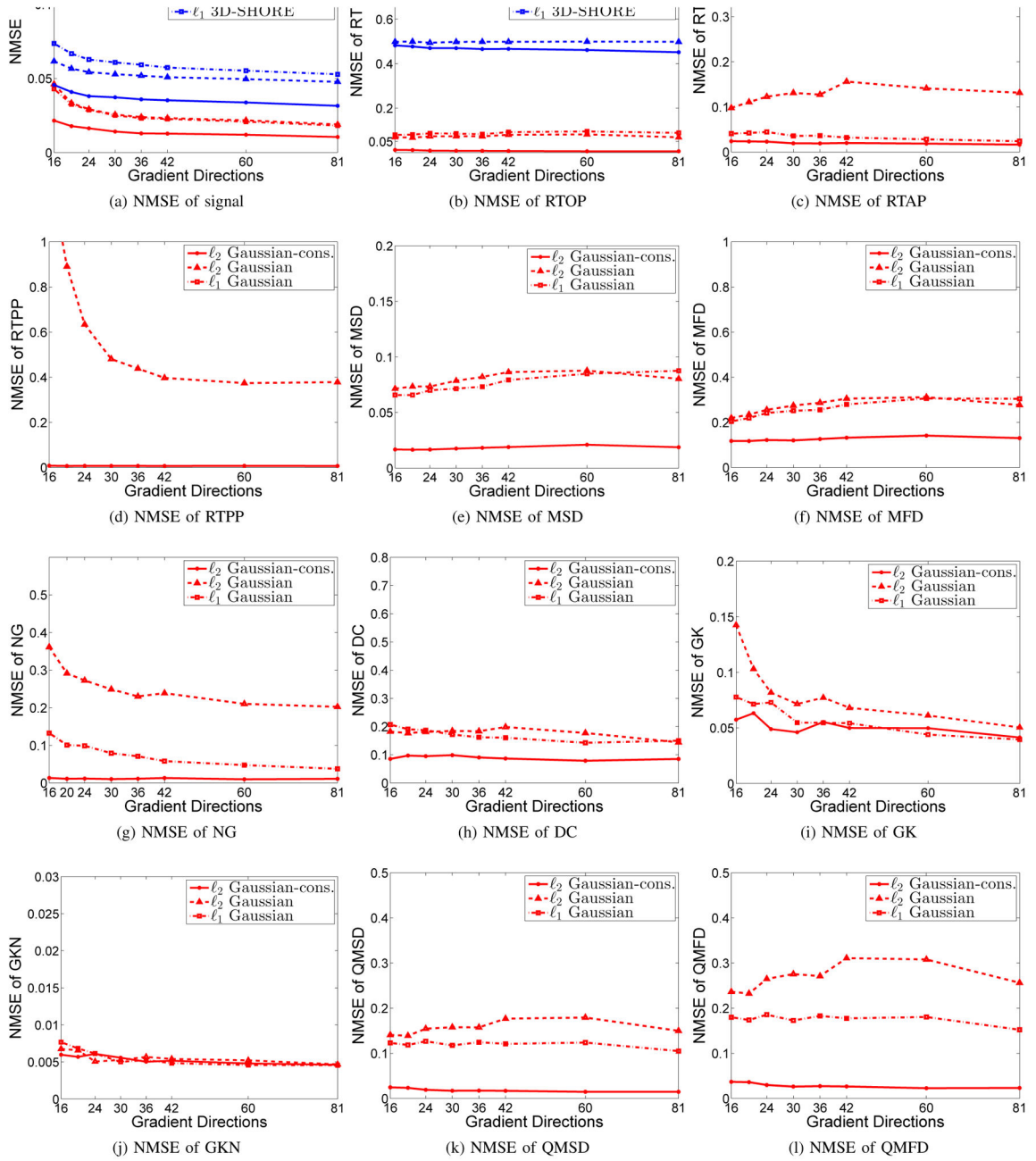


Fig. 9. Normalized-mean-squared errors using measurements on b-value shells with $b = \{1000, 3000\}$ vs. different number of gradient directions.

Author Manuscript

Author Manuscript

Author Manuscript

Author Manuscript

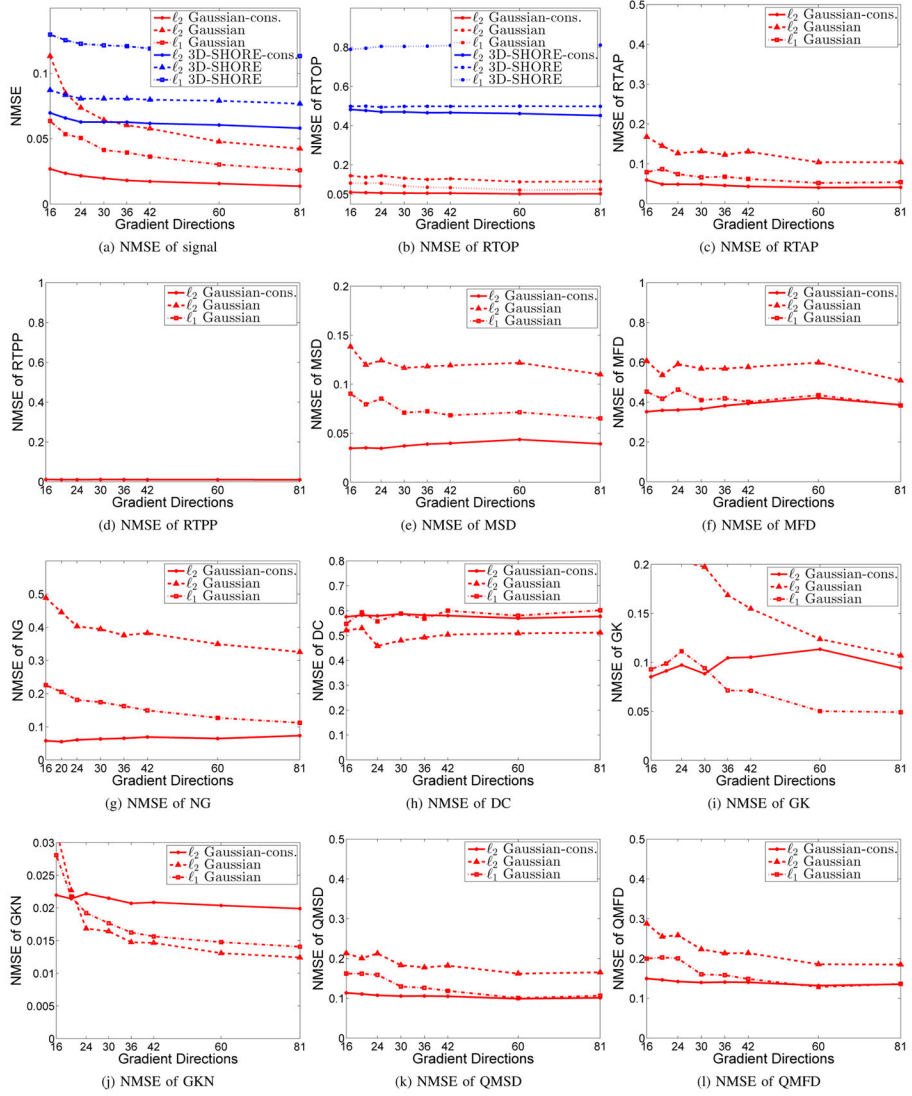


Fig. 10. Normalized-mean-squared errors using measurements on b-value shells with $b = \{1000, 2000\}$ vs. different number of gradient directions.

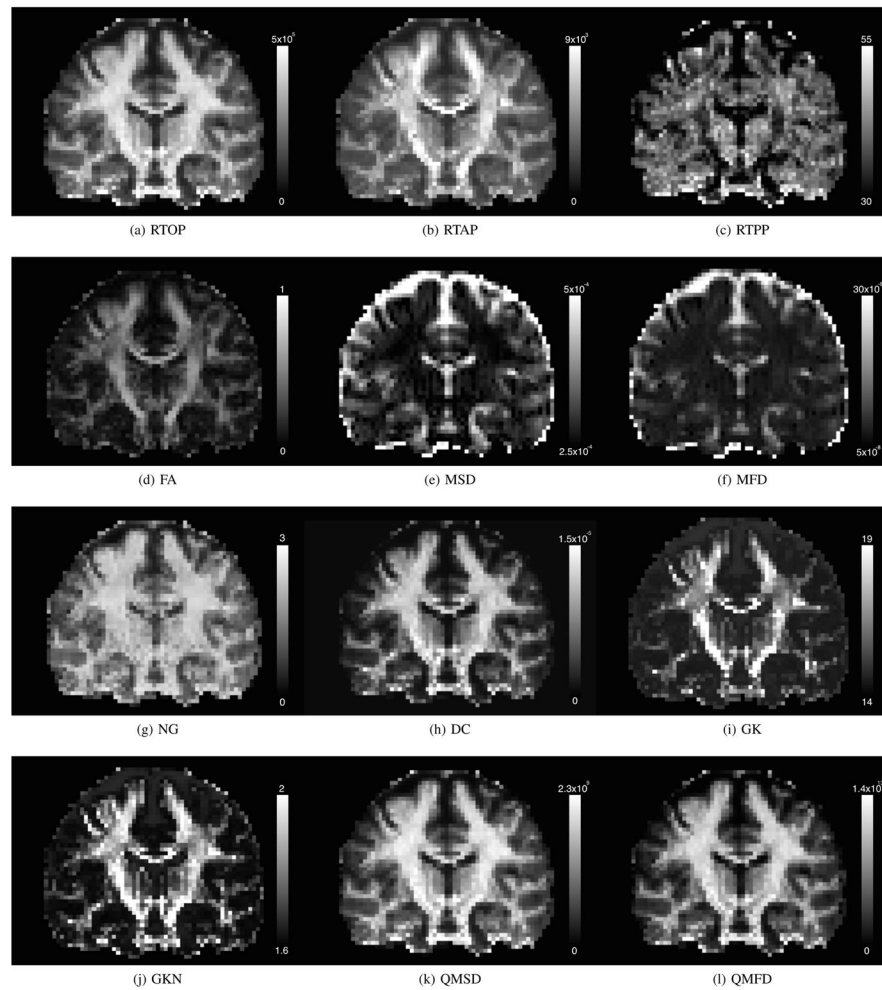


Fig. 11.

Estimated scalar indices for one coronal slice using the “gold-standard” data set: (a) return-to-the-origin probability (RTOP), (b) return-to-the-axis probability (RTAP), (c) return-to-the-plane probability (RTPP), (d) Fractional anisotropy (FA), (e) mean-squared-displacement (MSD), (f) mean-fourth-order-displacement (MFD), (g) non-Gaussianity (NG), (h) difference in covariances (DC), (i) general kurtosis (GK), (j) generalized kurtosis of the norm (GKN) of displacement, (k) q-space mean-squared-displacement (QMSD), (l) q-space mean-fourth-order-displacement (QMFD).

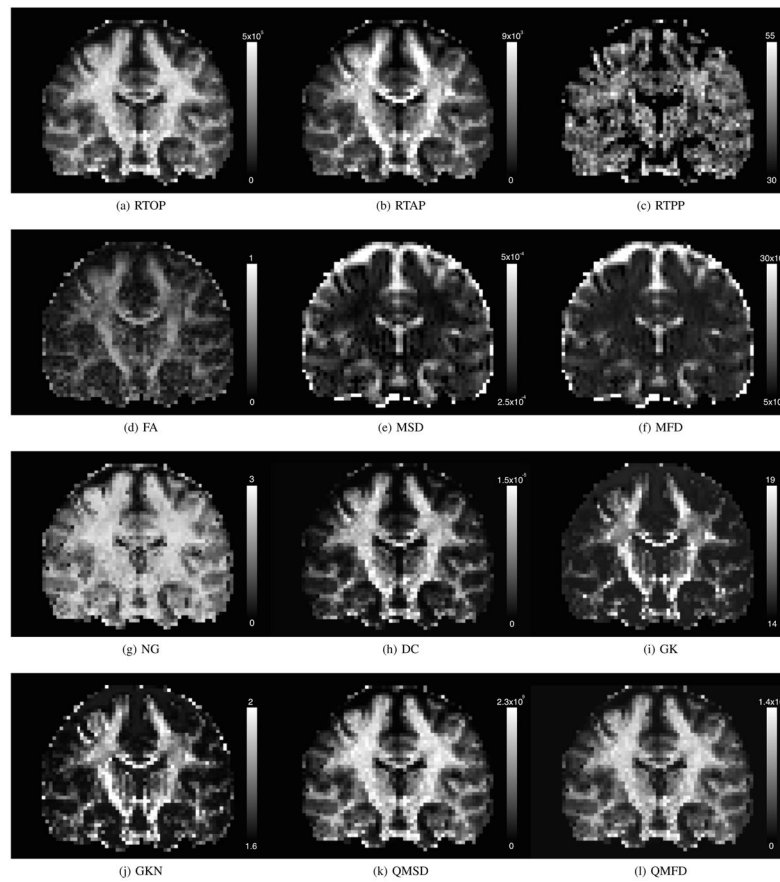


Fig. 12.

Estimated scalar indices for one coronal slice using measurements on b -value shells $b = \{900, 3600\}$ and 30 directions: (a) return-to-the-origin probability (RTOP), (b) return-to-the-axis probability (RTAP), (c) return-to-the-plane probability (RTPP), (d) Fractional anisotropy (FA), (e) mean-squared-displacement (MSD), (f) mean-fourth-order-displacement (MFD), (g) non-Gaussianity (NG), (h) difference in covariances (DC), (i) general kurtosis (GK), (j) general kurtosis of the norm (GKN) of displacement, (k) q-space mean-squared-displacement (QMSD), (l) q-space mean-fourth-order-displacement (QMFD).

TABLE I

The average SNR of the phantom data sets

	$b = 0$	$b = 1000$	$b = 2000$	$b = 3000$
single-fiber voxels	51	21	13	10
multiple-fiber voxels	26	15	11	9

TABLE II

Gold standard error metrics

Method	NMSE	EA	Method	NMSE	EA
ζ_1 Gaussian	0.5%	45.5°	ζ_1 3D-SHORE	0.3%	45.9°
ζ_2 Gaussian	0.5%	44.2°	ζ_2 3D-SHORE	1.0%	48.8°
ζ_2 Gaussian-cons.	1.1%	44.6°	ζ_2 3D-SHORE cons.	1.1%	48.7°

TABLE III

NMSE's using measurements with 30 gradient directions on two shells

b-value	NMSE of signal	NMSE of RTOP	NMSE of RTAP	NMSE of RTTP
{1000, 2000}	2.0%	5.6%	4.9%	1.1%
{1000, 3000}	1.4%	0.8%	1.9%	0.7%
b-value	NMSE of MSD	NMSE of MFD	NMSE of DC	NMSE of NG
{1000, 2000}	3.7%	36.6%	58.7%	6.3%
{1000, 3000}	1.8%	12.0%	9.9%	1.0%
b-value	NMSE of GK	NMSE of GKN	NMSE of QMSD	NMSE of QMFD
{1000, 2000}	8.8%	2.2%	10.6%	14.1%
{1000, 3000}	4.6%	0.6%	1.7%	2.7%

TABLE IV

Error metrics for $b = \{900, 3600\}$ and 30 directions per shell

	Gaussian			3D-SHORE		
	ℓ_2 -cons.	ℓ_2	ℓ_1	ℓ_2 -cons.	ℓ_2	ℓ_1
NMSE	3.9%	4.0%	3.5%	4.0%	5.9%	6.5%
NMSE of RTOP	0.7%	85.7%	48.8%	46.3%	44.0%	70.4%
NMSE of RTAP	1.4%	65.3%	31.0%	-	-	-
NMSE of RTPP	0.6%	12.6%	52.9%	-	-	-
NMSE of MSD	0.8%	10.7%	8.1%	-	-	-
NMSE of MFD	4.4%	26.0%	19.4%	-	-	-
NMSE of NG	1.1%	9.2%	6.4%	-	-	-
NMSE of DC	11.9%	> 100%	> 100%	-	-	-
NMSE of GK	0.2%	5.4%	3.3%	-	-	-
NMSE of GKN	0.1%	2.9%	1.7%	-	-	-
NMSE of QMSD	1.4%	42.4%	37.7%	-	-	-
NMSE of QMFD	1.8%	46.3%	41.4%	-	-	-

TABLE V

Error metrics for $b = \{900, 3600\}$ and 60 directions per shell

	Gaussian			3D-SHORE		
	ℓ_2 -cons.	ℓ_2	ℓ_1	ℓ_2 -cons.	ℓ_2	ℓ_1
NMSE	3.6%	3.1%	2.9%	3.6%	5.5%	6.2%
NMSE of RTOP	0.6%	72.5%	40.4%	45.3%	43.9%	71.0%
NMSE of RTAP	1.0%	41.4%	21.7%	-	-	-
NMSE of RTPP	0.4%	8.0%	29.1%	-	-	-
NMSE of MSD	0.8%	8.1%	8.5%	-	-	-
NMSE of MFD	4.7%	18.1%	21.7%	-	-	-
NMSE of NG	0.7%	5.6%	5.6%	-	-	-
NMSE of DC	12.2%	> 100%	> 100%	-	-	-
NMSE of GK	0.2%	4.5%	3.3%	-	-	-
NMSE of GKN	0.1%	2.9%	2.4%	-	-	-
NMSE of QMSD	1.2%	38.6%	30.3%	-	-	-
NMSE of QMFD	1.5%	41.6%	33.2%	-	-	-